Institut für Experimentalphysik I
Hadronenphysik

Search for Exotic Resonances in Antiproton-Proton Annihilation at Flight

MASTERARBEIT

im Studiengang "Master of Science" im Fach Physik
an der Fakultät für Physik und Astronomie
der Ruhr-Universität Bochum

vorgelegt von ERDEM KÖZ
geboren in Hagen
Bochum (2013)

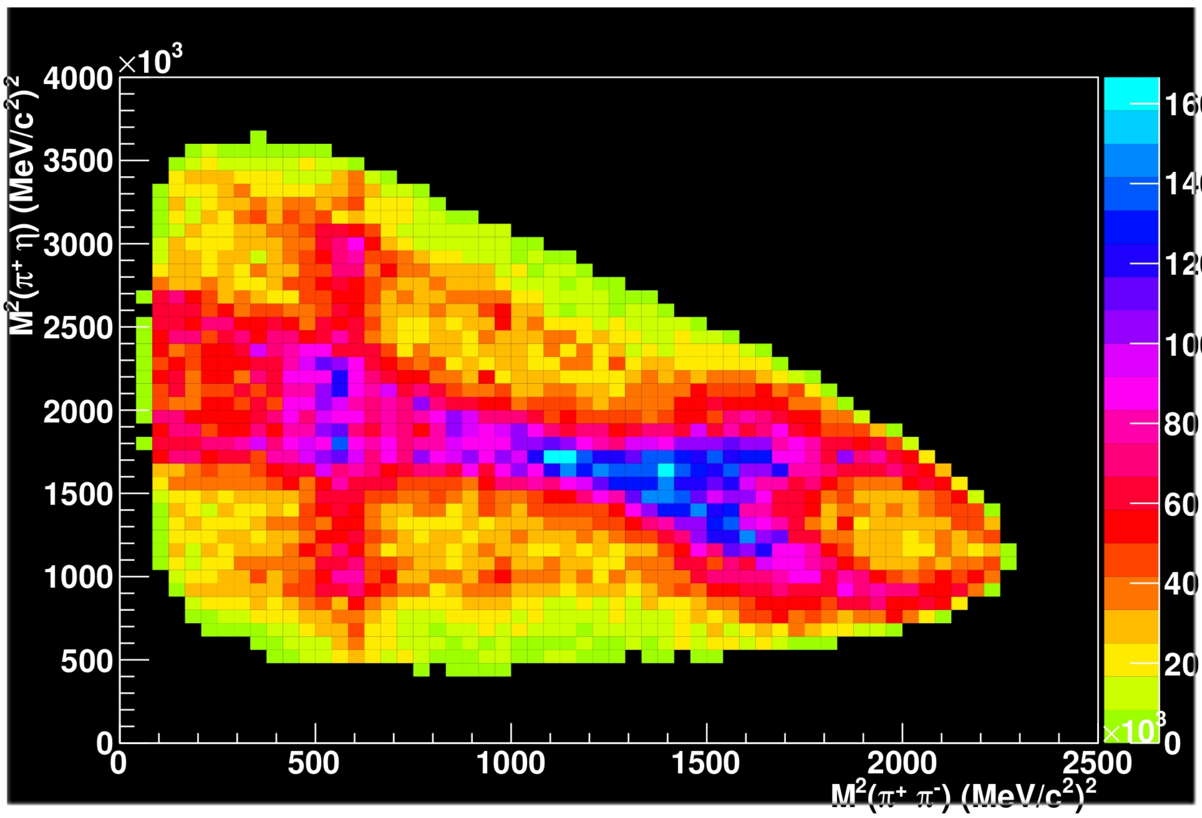

-

Eingereicht am 16.10.2013

1. Gutachter: Prof. Dr. Ulrich Wiedner

2. Gutachter: PD Dr. Fritz-Herbert Heinsius

Abstract

A partial wave analysis was done on the reaction $\overline{p}p \rightarrow \pi^+\pi^-\eta$ with data from the Cryrstal Barrel experiment at CERN. The data was taken at an $\overline{p}$-beam momentum of 900 MeV/c. The events from the raw data were selected by using various methods for background rejection. It was found that the highest contributing angular momentum is $L_{max} = 4$. The outcome of the partial wave analysis shows evidence for an exotic wave associated with the $\pi_1(1400)$ meson. It has the quantum numbers $J^{PC} = 1^{-+}$. The mass and the decay width of the $\pi_1(1400)$ were found to be $m_{\pi_1(1400)} = 1285.03 \pm 0.16\ MeV/c^2$ and $\Gamma_{\pi_1(1400)} = 136.03 \pm 0.32\ MeV$.

-

We can easily forgive a child who is afraid of the dark; the real tragedy of life is when men are afraid of the light.

Plato

-

Contents

List of Figures

List of Tables

1 Introduction

The field of high energy physics is a discipline that tries to uncover the mysteries of matter. The very constituents of matter are elementary particles that belong to two different groups of particles - the leptons and the quarks. The particles that belong to the group of leptons are the electrons (e^-), the myons (μ^-), the tauons (τ^-) and their corresponding neutrino particles. Many of them were found in particle physics experiments and some particles are created in many natural processes as well, like in cosmic radiation. The second group - the quarks - will be discussed later on in this chapter. The counterpart of matter is antimatter which is composed of antiparticles. Our present universe is completely made of matter, however, antimatter is still created and can also be produced with particle accelerators. Antimatter is stable but annihilates when it gets into contact with matter. The annihilation process releases a huge amount of energy.

The Standard Model of elementary particle physics is a theory that unifies the weak, strong and electromagnetic interactions. The force carriers of these interactions are the gauge bosons - the W and Z bosons for the weak interaction, gluons for the strong interaction and photons for the electromagnetic interaction. Some of their properties are listed in Table 1.1

Table 1.1: The fundamental interactions considered in the standard model with their corresponding charge and exchange particles.

Interaction	Charge	Exchange particle	Mass (GeV/c^2)	J^P
strong	colour	8 gluons (g)	0	1^-
weak	weak charge	$W^\pm, Z^0$	81, 91	1
electromagnetic	electrical charge	photon	0	1^-

The exchange particle of gravitation hasn't been found yet. The exchange particles of the strong interaction - the gluons - do interact with one another, because of their charge called colour. Gluons always carry two charge units - one colour charge and one anticolour charge. Taking into account that there are three colours (see section 1.1) and three anticolours and b) 9 gluons should exist, which can be grouped in a colour octet and a colour singlet state. The colour singlet state has not been observed so that only 8 gluons are considered as existing. The strong interaction takes place between quarks and has only an effect on short ranges ($\approx 10^{-15}$ m). It holds the protons and neutrons of a nucleus together and therefore makes up the very precondition for the existence of atoms. All particles that participate in the strong interaction are called hadrons. The weak interaction takes place between all fermions. Its exchange particles are the $W^{\pm}$ and Z^{0} bosons. Due to their heaviness the weak interaction has a short range. Its field strength is significantly less than that of the other two interactions and it is responsible for the β-decay.

1.1 Quarks

Quarks are strongly interacting particles that do interact by the weak and electromagnetic interactions. Since quarks only exist in bound states, free quarks cann't been observed directly. Evidences for quarks can be found in hadron spectroscopy, which will be explained in more detail later on, in lepton scattering and jet production.

Quarks are classified according to their quark numbers and *flavours* and are grouped in *generations*. There are six types of distinct flavours which are the *up* u, *down* d, *charm* c, *strange* s, *top* t and *bottom* b. They are written in pairs as it is given in 1.1.

$$Quark: \begin{pmatrix} u \\ d \end{pmatrix}, \begin{pmatrix} c \\ s \end{pmatrix}, \begin{pmatrix} t \\ b \end{pmatrix} \quad Antiquark: \begin{pmatrix} \overline{u} \\ \overline{d} \end{pmatrix}, \begin{pmatrix} \overline{c} \\ \overline{s} \end{pmatrix}, \begin{pmatrix} \overline{t} \\ \overline{b} \end{pmatrix}. \tag{1.1}$$

Each quark has its corresponding antiquark which are written at the right side in 1.1. Quarks have a non-integer charge in units of e. The u, c and t quarks and their antiquarks $\overline{u}$, $\overline{c}$ and $\overline{t}$ have a charge of $+\frac{2}{3}$ and $-\frac{2}{3}$, respectively. The quarks d, s, b and their antiquarks $\overline{d}$, $\overline{s}$ and $\overline{b}$ have a charge of $-\frac{1}{3}$ and $+\frac{1}{3}$, respectively. All quarks carry spin $\frac{1}{2}$ and belong therefore to the group of fermionic particles. The charge of quarks for the strong interaction is called colour which can adopt three possible values - *red*, *green* and *blue*. They are from now on referred to as r, g and b. Since free quarks haven't been observed yet, it is assumed that only colourless bound states can exist. Such states are for example a combination of three quarks each carrying one of the existing colour charges r, g or b. A quark-antiquark combination in which one carrys any colour and one the corresponding anticolour is possible as well. That is the composition of mesons of which an example is shown in figure 1.1. This rule is called colour confinement. Another important rule is the quark number conservation which says that in any electromagnetic and strong reaction the difference between the number of quarks and antiquarks with flavour f is constant. The exact formula for this rule is given in equation 1.2 where N_f is the total number, $N(f)$ the number of quarks with flavour f present and $N(\overline{f})$ the number of quarks with flavour $\overline{f}$ present. In weak interactions only the sum of all quarks have to be conserved with the

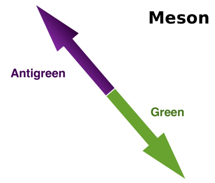

Figure 1.1: Example of a meson with green and antigreen as colour charge.

formula given in 1.3 where N_q is the total number of quarks, $N(q)$ the number of quarks present and $N(\overline{q})$ the number of antiquarks present.

$$N_f = N(f) - N(\overline{f}) \tag{1.2}$$

$$N_q = N(q) - N(\overline{q}) \tag{1.3}$$

Table 1.2 summarizes the most important properties of quarks. It is worth noting that the t quark compared with the other quarks has a very high mass of $\approx 171\ GeV/c^2$ compareable with that of a gold atom.

Table 1.2: Summary of important properties of quarks.

Generation	Symbol	Flavour	Charge	Mass (GeV/c^2)
1	u	Up	$+\frac{2}{3}$	$\approx 0.015 - 0.033$
	d	Down	$-\frac{1}{3}$	$\approx 0.035 - 0.060$
2	c	Charm	$+\frac{2}{3}$	≈ 0.1
	s	Strange	$-\frac{1}{3}$	≈ 0.5
3	t	Top	$+\frac{2}{3}$	≈ 171
	b	Bottom	$-\frac{1}{3}$	≈ 4.5

1.2 Quantum Chromodynamics

The theory of *Quantum Chromodynamics*, from now on referred to as QCD, is a gauge theory that describes the strong interaction. QCD says that the strong force is mediated by massless spin-1 bosons. Those bosons are called gluons which are in QCD the particles that correspond to photons in the theory of *Quantum Electrodynamics* (QED) which describes the electromagnetic force. One fundamental characteristic of the strong interaction is the asymptotic freedom. Asymptotic freedom is an effect in which the bonds between particles decrease by increasing the energy and analogously by decreasing the distance. This basically means that the force increases with increasing distance. That follows from the QCD coupling constant α_s which is given to a good approximation in equation 1.4, as well. In equation 1.4 N_f denotes the number of quark flavours and Λ is a parameter with a value of $\Lambda = 0.2 \pm 0.1\ GeV/c$.

$$\alpha_s = \frac{6\pi}{(33 - 2N_f)ln(\frac{\mu}{\Lambda})}$$
$$with \quad \mu^2 = |\vec{q}^{\,2} - \frac{E_q^2}{c^2}| \tag{1.4}$$

1.3 Hadrons and hadron spectroscopy

Hadrons are the bound states of quarks and hence are no elementary particles as they are compositions of even smaller particles. They are affected by the force field of the strong interaction. Hadrons themselves are subdivided into two groups - mesons and baryons. Baryons are made of three quarks or three antiquarks and mesons are made of a quark-antiquark pair. Furthermore baryons have half-integral spin whereas mesons have integral spin values. Hence the classification into baryons and mesons is made amongst others by their spin values and quark numbers.

The measurement of the properties of hadrons is called hadron spectroscopy. Those properties for example are their lifetimes, their masses, the values of their quantum numbers which are listed in Table 1.3, and so forth. It evolved as a consequence of studies on scattering experiments, in which resonances of particles could be found. It let to the assumption of the existence of quarks. Hadrons decay within a mean lifetime of $\tau = \frac{h}{2\pi\Gamma}$. Γ is called the decay width and is usally given in the unit MeV or GeV. Hadrons exist in families of charge multiplets. Particles that belong to the same charge multiplet have approximately equal masses but differ in their charge. An example of such a charge multiplett is the triplet of pions (π^+, π^0, π^-).

On the basis of the observations, it was thought that excited states of hadrons are similiar to the ones known from atomic and nuclear spectroscopy. As a consequence it was assumed that hadrons have to be a composition of even smaller elements. These smaller elements are called quarks. Hadrons have besides the usual quantum numbers of spin and parity addtionally quantum numbers that are listed in table 1.3.

The relationship between the quantum numbers of hadrons is described by the Gell-Mann-Nishijima formula which is given in equation 1.5.

$$Q = I_3 + \frac{1}{2}(B + S + C + b) \tag{1.5}$$

Table 1.3: All hadron quantum numbers.

Electrical charge Q
Baryon number b
Isospin I and its I_3 component
Strangeness S
Charm C
Bottom B
P-parity
C-parity
Spin

1.3.1 Mesons and exotic states

Mesons are particles, that were found in the first high energy particle collision experiments. They have as a rule a lifetime of approximately $\approx 10^{-8}s$ to $\approx 10^{-24}s$. At the end of their lifetime they can decay into lighter hadrons or leptons. Mesons can also decay into photons. Conventional mesons are composed of one quark-antiquark pair ($q\bar{q}$) and are subdivided for example into pseudoscalar mesons and vector mesons. Pseudoscalar mesons have a spin value of $J = 0$ and the spins of its quarks and antiquark are antiparallel to one another. Their parity is negative and is given by equation 1.6 with L the orbital angular momentum of the meson. Apart from this mesons have another form of parity which is called the C-parity and the G-parity. The operation of the C-parity which is called charge conjugation has the effect of reversing all additive quantum numbers like the electrical charge e, baryonnumber b, leptonnumber l, strangeness S, and so forth. C-Parity basically says whether the wave-function of the meson remains the same after changing the quark with its antiquark and vice versa. It is given by equation 1.7. The operation of G-parity which is a generalization of C-parity is defined by a charge conjugation with an additional rotation around the I_2-axis by an angle of π. The operation is given by equation 1.9 whereas G-Parity is given by equation 1.8.

$$P = (-1)^{L+1} \tag{1.6}$$

$$C = (-1)^{L+S} \tag{1.7}$$

$$G = (-1)^{L+S+I} \tag{1.8}$$

$$G_{op} = Ce^{i\pi I_2} \tag{1.9}$$

The theory of Quantum Chromodynamics that was introduced earlier in this chapter suggests on the basis of the MIT-Bag-model in addition to the existence of baryons and mesons the existence of multiquark states, quark-gluon-states and glueballs. Those states are called exotic states and can be grouped as follows:

- **Multiquark states** are a composition of multiple quark-antiquark-pairs ($\overline{q}^k q^k$). Multiquark states can be classified according to k. Common classes are baryonia with k=3 and diquonia with k=2.
- **Hybrids** are a composition of one quark-antiquark-pair and additional gluonic degrees of freedom ($\overline{q}qg^k$ with $k = 1, 2, ...$) instead of virtual gluons in conventional mesons.
- **Glueballs** are states composed solely of gluons. They exist in states of at least two gluons (gg) or more (ggg ...). According to QCD the gluons themselves are bound together by the exchange of virtual gluons.

π-meson

Pions are composed of quark-antiquark pairs, and thus belong to the group of mesons. The pion was discovered after the proton and neutron, being the third discovered hadron. There are three kinds of pions - the π^+, π^- and π^0. The latter one is not charged, whereas the π^+ and π^- have a positive and negative charge, respectively. The various pions are composed of quarks as follows:

$$|\pi^+\rangle = |u\bar{d}\rangle \tag{1.10}$$

$$|\pi^-\rangle = |\bar{u}d\rangle \tag{1.11}$$

$$|\pi^0\rangle = |\frac{u\bar{u} - d\bar{d}}{\sqrt{2}}\rangle \tag{1.12}$$

Positively charged pions, for example, can be produced through the reaction $p + p \rightarrow p + n + \pi^+$.

η-meson

The η-meson was discovered in 1961 and has a mass of 547,85 MeV/c^2. It is a combination of up-, down- and strange quark-antiquark pairs as follows.

$$|\eta\rangle = |\frac{u\bar{u} + d\bar{d} + s\bar{s}}{\sqrt{6}}\rangle \tag{1.13}$$

The η-meson is not charged and has no corresponding antiparticle.

$\pi_1(1400)$

The $\pi_1(1400)$ is an exotic meson, i.e. a non-$\bar{q}q$ meson with current parameters given in Table 1.4. First hints for the existence of the $\pi_1(1400)$ ocurred at the GAMS collaboration but were not sufficient to proof its existence. Later on the Crystal Barrel experiment, which amongst other things was aimed at finding exotic states (see chapter 2), found evidences for the existence of the $\pi_1(1400)$. The evidences were discovered in the following reaction channels:

- $\bar{p}n$ annihilation at rest into $\pi^-\pi^0\eta$
- $\bar{p}p$ annihilation at rest into $\pi^0\pi^0\eta$

It was seen in both cases as an exotic state decaying into $\pi\eta$ with quantum numbers $I^G = 1^-$ and $J^{PC} = 1^{-+}$. Since $I^G = 1^-$ the resonance can't be a glueball but is probably a hybrid ($q\bar{q}g$) or a four-quark state ($q\bar{q}q\bar{q}$). The mass that was determined in the former reaction was $m = 1400 \pm 20\,MeV/c^2$ whereas in the latter it was determined at $m = 1360 \pm 25\,MeV/c^2$. The value given in Table 1.4 is the weighted average of [PDG2013] that also accounts for the values of other experiments in which it was seen.

Table 1.4: Current values for the parameters of the $\pi_1(1400)$.

π_1(1400)	
Mass (MeV/c^2)	1354 ± 25
Decay width (MeV)	330 ± 35

Most of the information in this chapter can be extracted from [Mar2009], [Pov2009] and [PDG2013].

1.4 Motivation

The main goal of this thesis is to identify intermediate resonances and to determine their properties like masses, widths and quantum numbers for the reaction $\bar{p}p \rightarrow \pi^+\pi^-\eta \rightarrow \pi^+\pi^-(\gamma\gamma)$. The data was taken with the Crystal Barrel experiment at CERN from an of the antiproton-proton-annihilation in flight at an $\bar{p}$ momentum of 900 MeV/c. The Channel $\bar{p}p \rightarrow \pi^+\pi^-\eta \rightarrow \pi^+\pi^-(\gamma\gamma)$ bears the possibility of the existence of a resonance X with an exotic quantum number combination for the reaction chain $\bar{p}p \rightarrow X\eta$ with $X \rightarrow \pi\eta$. That system can have a spin-parity-value of $J^{PC} = 1^{-+}$ and an isospin value of $I = 1$. Observing these values would confirm the existence of an exotic state. Furthermore, this thesis is the first to study on the $\pi^+\pi^-\eta$ final state produced in $\bar{p}p$-annihilation in flight. A possible candidate for this exotic state could be the $\pi_1(1400)$ or the $\pi_1(1600)$ (see previous subsection).

The event reconstruction and data selection is aimed at preparing the data for the partial wave analysis. The partial wave analysis is necessary in order to identify the intermediate states and to determine the properties of the reaction channel $\bar{p}p \rightarrow \pi^+\pi^-\eta$. Apart from this, the thesis is a part of studies that are conducted for the $\overline{P}ANDA$-experiment and the test of the partial wave analysis tool *PAWIAN*, as well.

1.4.1 $\bar{P}$ANDA-Experiment

This section gives an overview of the $\overline{P}$ANDA-Experiment since it is a part of the motivation behind this thesis. More detailed information on the $\overline{P}$ANDA-experiment can be obtained in [Kra2012] and in [PAN2009]. The $\overline{P}$ANDA[1]-Experiment is part of the accelerator complex FAIR[2] which is currently built at GSI[3] in Darmstadt, Germany. FAIR will be composed of multiple accelerators, storage rings etc. on which multiple experiments will be conducted in the future. One of the core components of the accelerator complex will be the storage ring HESR[4] which will have the function of storing the antiprotons ($\bar{p}$). The stored $\bar{p}$-s will have momenta in the range from 1.5 GeV/c up to 15 GeV/c using stochastic and electron cooling. The $\bar{p}$-s themselves will be produced by a 30 GeV/c proton-beam. Experiments can be done on two possible resolutions of the beam-momenta with $\frac{\Delta p}{p} \approx 10^{-4}$ and $\frac{\Delta p}{p} \approx 2 \cdot 10^{-5}$. Choosing the lower momentum resolution makes it possible to conduct the experiment with a higher luminosity of $2 \cdot 10^{32}\ cm^{-2}s^{-1}$ while a high resolution leads to a lower luminosity of $2 \cdot 10^{31}\ cm^{-2}s^{-1}$.

[1] AntiProton ANnihilations at DArmstadt
[2] Facility for Antiproton and Ion Research
[3] Gesellschaft für SchwerIonenforschung
[4] High Energy Storage Ring

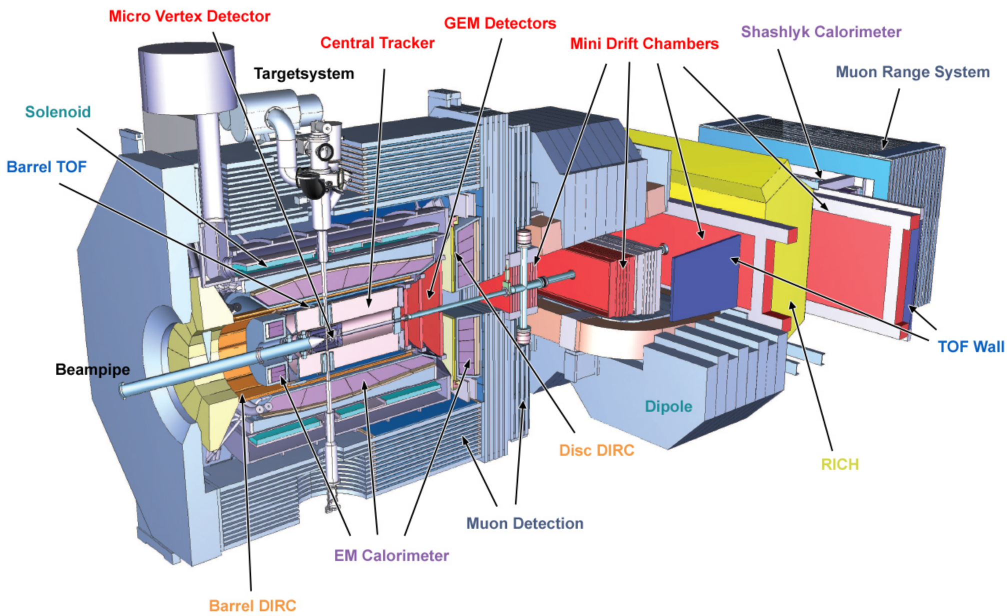

Figure 1.2: Depiction of the PANDA-detector.

Another core component is the detector which can be subdivided into two parts which are the Target Spectrometer and the Forward Spectrometer (see figure 1.2). The target can be a frozen hydrogen pellet target, a cluster-jet target or a solid target. One of the main goals of the $\overline{P}$ANDA experiment will be the search for glueballs and hybrids, the spectroscopy of charmonium[5]- and open-charm-states.

[5] $c\bar{c}$-mesons

2 Crystal Barrel Experiment

The data that is studied in this thesis was taken at the Crystal Barrel Experiment which was an experiment in CERN[1] the european center for nuclear research in Switzerland, Geneva, and partly also in France. The Crystal Barrel experiment was operated in the year between 1989 - 1996 and was an experiment aimed at researching the $\overline{p}p$-annihilation at rest and in flight. Its maximum beam momentum was 1940 MeV/c. The physics program of the Crystal Barrel experiment consisted of three main topics which were the following:

- Spectroscopy of light mesons
- Search for exotic states like glueballs, hybrids and baryonia
- Studies on the $\overline{p}p$-annihilation mechanism

This chapter gives a glance of the important components of the experiment. Detailed information on the Crystal Barrel experiment can be found in [CBL1992] and the figures used in this chapter are available in [CB2013].

2.1 LEAR and the production of antiprotons

The antiprotons in the Crystal Barral Experiment were produced at the accelerator complex at CERN. The production of the antiprotons was a process consisting of six phases. In the first phase protons were accelerated in the LINAC which is a linear accelerator and afterwards the protons got injected into the proton synchroton booster (PSB) and the proton synchroton (PS). After all three accelerators have been passed the protons leave the PS with an energy of 26 GeV. The production of the antiprotons is then done according to the reaction that is given in Equation 2.1. The collision of two protons results in the production of an extra proton and an extra antiproton.

$$p + p \rightarrow p + p + p + \overline{p} \tag{2.1}$$

[1] Conseil Européen pour la Recherche Nucléaire

The second proton in reaction 2.1 is given by a tungsten target directing the proton from the PS on the tungsten. The antiprotons, after being seperated from the protons, are then injected into the antiproton accumulator (AA). The AA is an intermediate storage ring that reduces the phace space of the antiprotons by means of stochastic cooling. The antiprotons again pass the PS for deacceleration to a momentum between 600 MeV/c and 1949 MeV/c. The antiprotons are then injected into the LEAR[2]. LEAR uses electron and stochastic cooling as well. Figure 2.1 depicts the complete accelerator complex as it was when the Crystal Barrel experiment was conducted.

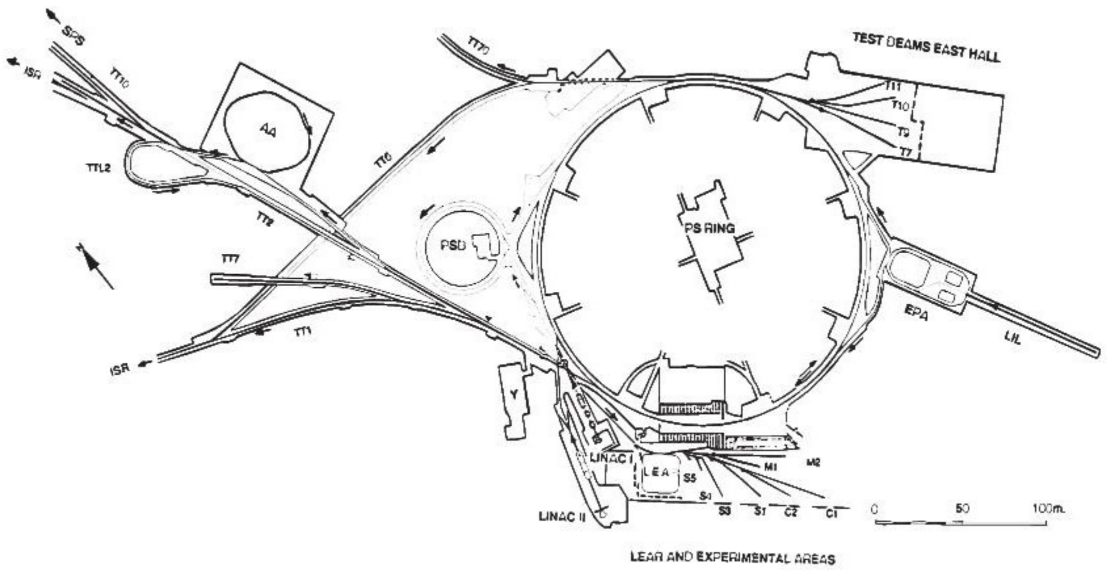

Figure 2.1: The accelerator complex at CERN. The LEAR storage ring is depicted in the lower part of the figure.

2.2 Crystal Barrel Detector

The Crystal Barrel detector was a multi-component detector which was able to simultanously detect neutral and charged particles and provided an acceptance of ≈ 98.7 % 4π for neutral particles. The acceptance for charged particles is lower since jet drift chamber and the silicon vertex detector covered a smaller angle. The detector had no specific PID detectors like a Cerenkov detector or a Time of Flight detector. The identification of the particles was still possible by the measuring of $\frac{dE}{dx}$. In order to achieve the goals of the above mentioned physics program the detector had to fulfill important requirements. Some of which were to have low background noise and high resolutions for important measures like the energy and momentum. The detector itself had a target in its center with the $\overline{p}$-beam coming from the left in Figure 2.2. Furthermore, it consisted of the silicon

[2]Low Energy Antiproton Ring-storage

vertex detector, the jet drift chamber, the barrel calorimeter, the aluminium coils, and the magnet yokes. The most important of these components are to be described in more detail in the following sections.

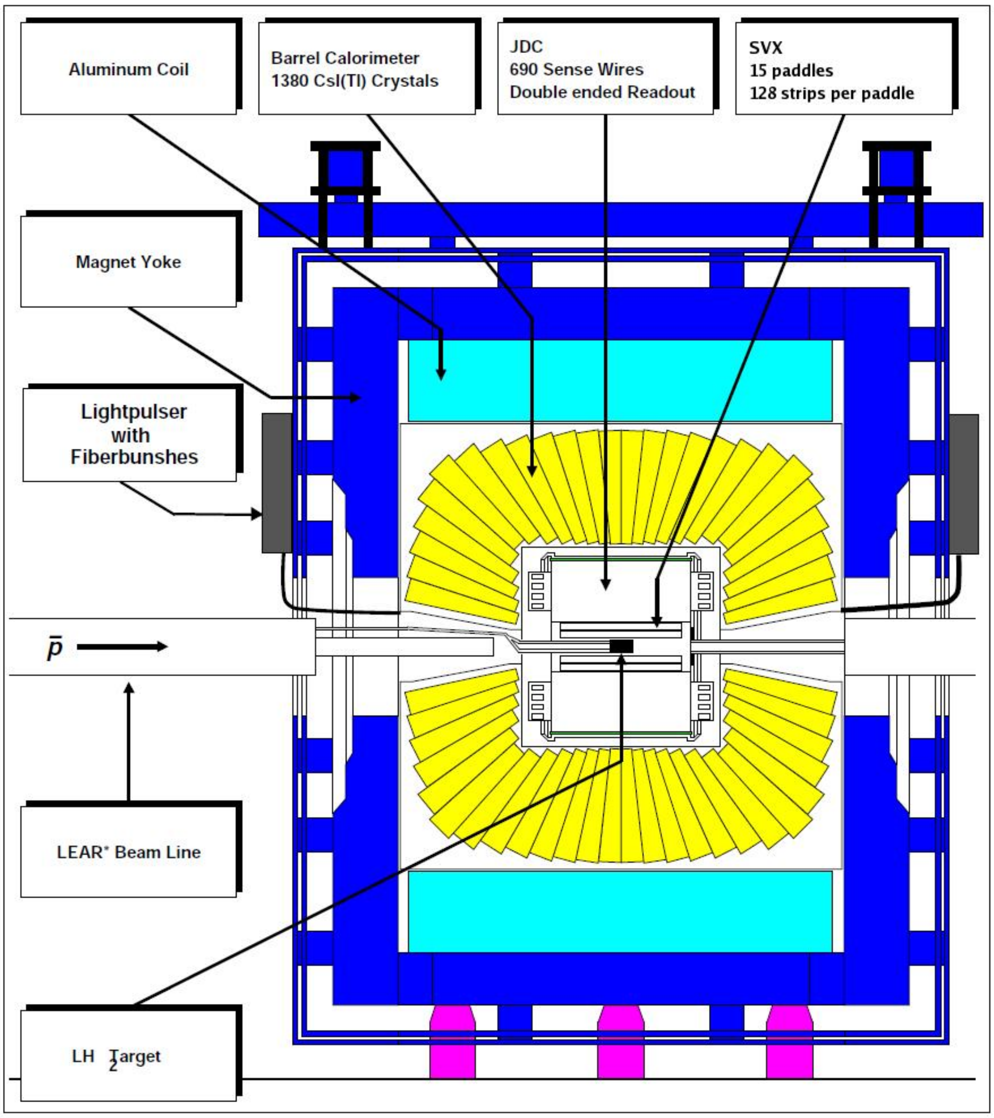

Figure 2.2: Schematic depiction of the Crystal Barrel detector (CBD).

2.2.1 Target

As can be seen in Figure 2.2 the target is located in the center of the detector where from the left on that figure the antiproton beam is directed on the target. The targets that were used in the experiment were mostly liquid hydrogen LH_2, LD_2 and hydrogen gas H_2. The LH_2 target was the target that was used for $\bar{p}p$-annihilation in flight. The rates for an annihilation to occur starts at about 1.4 % at a beam momentum of 600 MeV/c and goes down to 0.8 % at the maximum beam momentum of 1940 MeV/c.

2.2.2 Silicon Vertex Detector

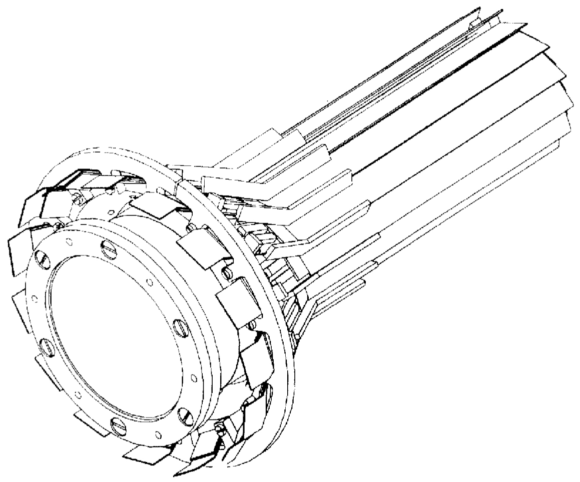

Figure 2.3: Silicon vertex detector (SVX).

The silicon vertex detector (SVX) surrounds the target and is surrounded by the jet drift chamber. The purpose of the SVX is to detect the amount of charged particles that are created by the $\overline{p}p$-annihilation. It is quick by still having a high acceptance value. In addition to this the SVX has a high spatial resolution since the distance between the plates is only 50 μm thick which makes it possible to localize the annihilation vertex. The SVX consisted of 15 SiO_2-plates that were arranged like a cylinder as can be seen in Figure 2.3. The cylinder has a length of 75 mm and a radius of 40 mm. The SVX was in use from 1995. Prior to it a proportional wire chamber was used.

2.2.3 The Jet Drift Chamber

The Jet Drift Chamber measures the trajectory of the charged particles. A magnetic field that is adapted in the direction of the beam axis causes a curvature. The magnetic field has a strength of 1.5 T. The trajectories are detected by the interaction of the charged particles with the gas. The gases that were used in the JDC were carbon dioxide and isobutane. With the curvature of the trajectory it is possible to determine the momentum of charged particles. The Jet Drift Chamber surrounds the silicon vertex detector and is surrounded itself by the calorimeter as can be seen in figure 2.2. The JDC has a cylindrical shape and consists of wires. The wires subdivide the JDC into 30 sectors as can be seen in Figure 2.4. In that figure an enlargement of the sectors is depicted which are lined by the wires. It shows that the wires are not arranged as straight lines but are displaced by 0.2 mm from one another. This is due to the ambiguity that is caused by a particle that goes through the JDC by passing only one sector. In that case it wouldn't be possible to determine whether the particle crosses the wires from the left or from the right if the wires were arranged as straight lines. The wires have a distance of 8 mm to one another.

The coordinates are then allocted to their actual trajectories and the trajectories on the other hand are fitted in with a helix. The helix has five free parameters of which the following three are relevant for this thesis:

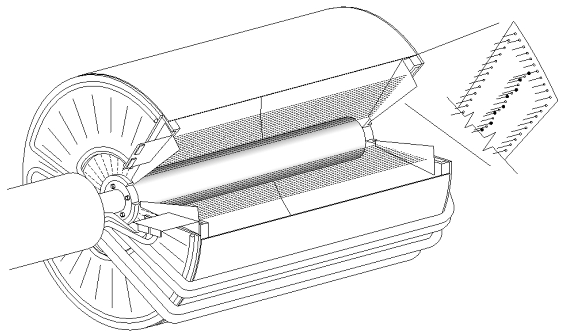

Figure 2.4: Schematic depiction of the JDC.

- The curvature of the Helix α
- The angle between the x-axis and the rΦ-projection Ψ_0
- The angle of inclination λ

The four-momentum can be obtained with these three parameters, the absolute value of the momentum $p = p_t \sqrt{1 + tan^2\lambda}$ and the transversal momentum $p_t = \frac{qB}{\alpha}$

$$P = \begin{pmatrix} \sqrt{m^2 + p^2} \\ p_t \cos \Psi_0 \\ p_t \sin \Psi_0 \\ p_t \tan \lambda \end{pmatrix} \tag{2.2}$$

where m is the mass and q the charge of the particle and B the magnetic field. The JDC is also used to seperate between pions and kaons by measuring $\frac{dE}{dx}$.

2.2.4 Calorimeter

A calorimeter is used to detect photons thus making it the most important component of the detector. The calorimeter of the Crystal Barrel detector is denoted by CB. It is laid out as a barrel consisting of 1380 CsI(Tl) crystals. It was positioned such that the target was exactly in the center of the barrel. A schematic depiction of it is given in Figure 2.5. The CB surrounds the JDC completely which can be seen in figure 2.2 where CB is coloured yellow. In order to retain the symmetry of the CB, exactly 13 types of crystals are required. The crystals are arranged in such a way that the crystals in azimutal direction cover 6° (type 1) each and those in polar direction cover 12° (type 2) each. The calorimeter covers a spatial angle of $\approx 98.7\% \cdot 4\pi$ for uncharged particles. The coverage for charged particles isn't that high and lays at $\approx 95.2\% \cdot 4\pi$. The resolution of the energy of the CB is given by formulae 2.3 where E is given in GeV.

$$\frac{\sigma_E}{E} = \frac{2-3\%}{(E)^{\frac{1}{4}}} \tag{2.3}$$

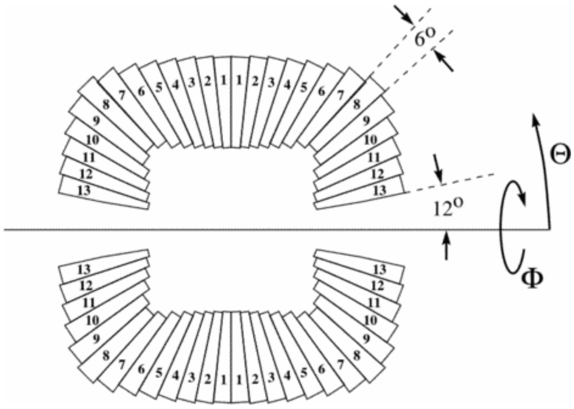

Figure 2.5: The arrangement of the CsI(TI) crystals forming the crystal barrel.

The spatial resolution has a value of 20 *mrad* in both - Φ and Θ - direction. The complete CB construction with all crystals had a weight of 4 *t*.

CsI(TI) crystals

The cystals that are used for the calorimeter are thallium-dotated (Tl) caesium-iodid crystals (CsI). They have a length of 30 *cm* which makes it possible to deponate photons up to 2 *GeV*. Furthermore it has a 100 μ*m* thick titan cover which serves as a protection giving the crystal more stability and protecting the readout electronics from electrical influences coming from the environment etc. The rear parts of the crystals have the readout electronics attached (2, 3, 4 and 7 in Figure 2.6). The readouts used photodiodes for the detection of photons since photodiodes are not influenced by the magnetic field. Before the photons can be detected by the photomultiplier they have to pass the wave-length-shifter (6) in Figure 2.6.

These wavelength shifters shift the wavelength of light that are emitted by the crystals in a wavelength area that is readable by the photodiodes.

2.2.5 Trigger system and data recording

The function of the trigger system was to record only events that were of interest. The reason for the necessity of a trigger system in detectors in general is the huge amount of data that is produced during the experiments which can't all be stored but have to

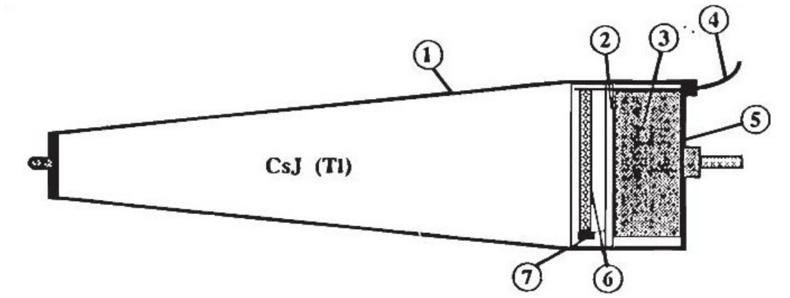

Figure 2.6: Schematic depiction of a CsI(Tl)-crystal of the calorimeter with the following components: 1) Titan cover, 2) and 3) circuit board, 4) optical fibre, 5) protective cap, 6) wave length shifter, 7) photodiode

be filtered. The trigger system of the Crystal Barrel experiment consisted of multiple levels as can be seen in Figure 2.7. In each level the number of events was reduced by one order of dimension. Level 0 and 1 were sole hardware trigger. Level 0 assured that every event registered originated from an $\overline{p}p$-annilation by counting every incoming $\overline{p}$. A second counter behind the target registered every outgoing $\overline{p}$ which was the signal that no $\overline{p}p$-annihilation took place. The filter criterion of the level 1 trigger was the multiplicity value for the detected charged and uncharged particles which was compared with the expected value. Level 3, which is the last level of the trigger system, is a software based trigger. It calculates the four-vectors and reconstructs π^0- and η-mesons. The time to pass the whole trigger system could take ≈ 1 ms. The level 3 trigger was not used in the data used in this thesis. Level 0 makes 0.1 μs, level 1 makes 10 μs and level 2 makes up to 1000 μs of this time.

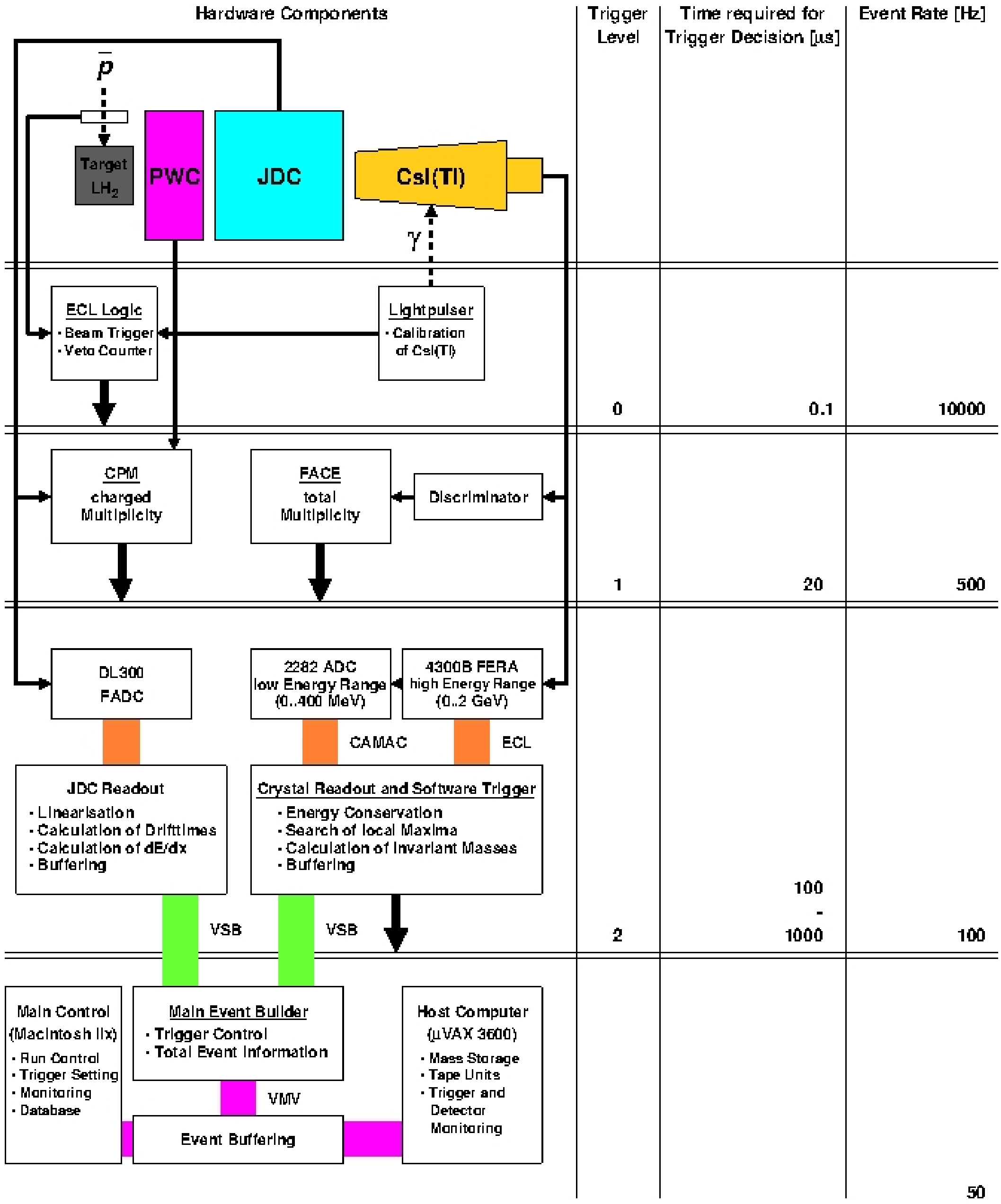

Figure 2.7: A schematic sketch of the trigger system as it was used in the Crystal Barrel experiment.

3 Event reconstruction and data selection

The purpose of the event reconstruction and selection is to prepare the raw data for a thorough analysis and especially the partial-wave-analysis. The particles have to be identified and structured because the required four-vectors of the mesons were not measured directly. Instead of directly detected resonances the data includes only the deay products like the photons detected by the calorimeter. The whole process from event reconstruction to the data selection makes use of multiple software packages. The most important are the following software packages:

- **LOCATER**, used to reconstruct the tracks of charged particles.
- **BCTRAK**, responsible for the analysis of the measurements of the calorimeter.
- **GTRACK**, merges the results of the software packages LOCATER and BCTRACK for every event to a single record.
- **GEANT**, used to simulate Monte Carlo events by propagating each particle through a defined detector in the detector, respectively.
- **CBGEANT**, is based on GEANT and is customized to the crystal barrel detector.
- **CBOFF++**, is the interface between the software packages written in FORTRAN and the analysis software written in C++.
- **Brain**, is a neural network for the detection of electromagnetic splitoffs.
- **ROOT**, is a comprehensive library of C++ classes for the analysis of vast data volumes.

The main part of this chapter focuses on the description how to separate background events from signal events. Various methods and techniques will be used amongst of which will be the event based rejection method.

3.1 Identification of photons in the calorimeter

The photons, created through the various particle decays, penetrate the crystals of the detector and excite them mainly by pair production and by bremsstrahlung but also by the photoeffect. As a consequence the so called electromagnetic showers occur. These electromagnetic showers are converted into light within the crystals and the light is converted into electric signals and then are processed by the readout electronics. Photons with high energies can cause electromagnetic showers that are able to reach neighbouring crystals. To still be able to determine the place of origin and the exact energy that was deposited, the crystals are grouped to clusters. These clusters are then searched for energy maxima. The deposited energy of the photons are then determined through the use of calibration constants whereas the flight direction is determined by the spatial location of the cluster. In order to suppress the background caused by the readout electronics on the crystals it is necessary to set energy thresholds. Those energy thresholds are listed in table 3.1. These values are based to some extend on values from prior works for example in [Beu1995]. The events of the data that is analyzed in this thesis are 2-Prong[1] events. The value for the minimum energy of a crystal is set at 1 MeV and can be extracted from Table 3.1. Crystals below that energy are not considered. The standard of a coherent cluster is 10 MeV. Therefore the minimum energy of a crysal in a cluster must be 4 MeV to be considered as the starting point in the reconstruction. The central crystal of a local energy maximum must be 20 MeV to be considered as a energy deposition of an independent particle. Such an energy maximum is called a PED (Particle Energy Deposit). The threshold for a crystal within a cluster has to be 4 MeV otherwise it is not considered as part of a cluster. An energy maximum is considered a PED if it has an deposited energy higher than 20 MeV.

Table 3.1: Various energy thresholds to suppress background.

Threshold	2-Prong(MeV)	Purpose
E_{XTAL}	1	Suppression of the background from the readout electronics
E_{CLU}	20	The total energy of a cluster in order to be detected as one
E_{CLS}	4	A cystal within a cluster needs to have this energy at least
E_{PED}	20	The energy that a PED has to have at least

[1]The name n-prong denotes with n the number of charged particles.

3.1.1 Electromagnetic and hadronic splitoffs

Because the spread of electromagnetic showers are caused by statistical processes it is possible that more than one energy maximum may occur through one photon. The shower fluctuations can even expand so far that multiple clusters occur. This is called a electromagnetic splitoff. This can lead to the reconstruction of wrong photon candidates. To suppress electromagnetic splitoffs it is not recommended to use the method of energy thresholds, because it would also suppress low energy photons. Instead artificial neural networks are used to distinguish between splitoffs and real photons. The recognition is done by the neural network software BRAIN. Another form of splitoffs are the hadronic splitoffs. The difference to electromagnetic splitoffs is that hadronic splitoffs are caused by hadrons. To detect hadronic splitoffs, artificial neutral networks are used as well by using the software JHONNY WALKER.

3.2 Data selection

The raw data that will be examined in this thesis was recorded in September 1996 at the Crystal Barrel experiment at CERN in Geneva, Switzerland. The raw data contains charged and uncharged particles with a total event momentum of 900 MeV/c and consists of about $\approx$ 14.9 million events. As a preliminary work it is necessary to remove as much background as possible from the raw data.

3.3 Preselection

The preselection of the raw data is of great importance to the whole analysis process. The goal of the preselection is to reduce as much unuseful data and background as possible in order to decrease the data volume that later has to be analyzed in more detail and thus will need much more computing power. In the preselection phase data is subjected to a couple of conditions that determine whether an event can pass or not. These conditions are applied in a multi-stage approach. These stages are the following:

- **Total charge**
  Charge conservation law requires the total charge for $p\bar{p}$ events to be zero.

- **Charged particles**
  The amount of charged particles must be two, which means that exactly one positive and one negative charged particle have to be considered.

- **Number of photons**
  The number of photons must be two in the final state

- **Energy and momentum**
  Conservation of the total momenta and energy must be given with $\Delta\vec{p} = |p_{event} - p_{beam}| < 200\ MeV/c$ and $\Delta E = |E_{event} - E_{\bar{p}p}| < 400\ MeV$

- **Z-vertex cut**
  The z-vertex must be within the target.

Applying all selection stages gives the statistics listed in table 3.2. The goal to decrease the background volume from the data significantly is achieved. The total data decreased by about 95 % compared with the number of events of $\approx$ 14.9 million given before the preselection. The fact that it is possible that also relevant data will be cut out makes a study on Monte Carlo generated events with the final state $\pi^+\pi^-\eta$ necessary. Studies on Monte Carlo generated events are dealt with in section 3.6. The first selection stage, where only final states with 2 charged particles are allowed to pass, decreases the number of events by$\approx$ 30 %. This is probably due to the fact that the creation of uncharged pions and Kaons cover a great share on all events leading to uncharged final states like $\pi^0\pi^0$ which are filtered out in the first preselection stage. The second stage leads to a decrease of an additional 10 % of the data which is compared with the first stage not a great leap. A conclusion that can be made from this is that most of the produced events that lead to a final state with two charged particles are composed of a negatively and a positively charged particle. The third stage that pass only events leading to a final state with 2 photons candidates has the the greatest decrease in data volume. An additional share of $\approx$ 50 % is cut out by the third stage. Figure 3.1 shows the invariant-$\gamma\gamma$ mass spectrum after the whole preselection process. The spectrum has two resonances with the first resonance as the dominant one. The first resonance corresponds to neutral pions and it can be concluded that pions have the greates share on the data. The last two cuts (events inside energy window, events inside momentum window) result in an insignificantly small amount of cut-out-events. The energy window cut and momentum window lead to a decrease of an additional $\approx$ 4 % leaving the preselection at 670122 events which make up $\approx$ 5 % of the originally given events.

Z-vertex cut

The last cut of the preselection considers the z-vertex. In Table 3.2 it is listed that the events are decreased by an additional $\approx$ 0.10% as a result of the z-vertex cut. Figures 3.2 and 3.3 give a glance at these events which are not within the z-vertex and how they are distributed over the plane. Most of these events lie at between $\approx$ 10 - 15 cm with a peak at

$z \approx 12$ cm in figure 3.2. A better insight on how the cut-out events are distributed over the y-z-plane can be gained from figure 3.3. It reveals that events which were cut out from the area from $z \approx -8\ cm$ downwards are quite equally distributed over the y-z-vertex-plane with a relatively little increasing number of events going up from $z \approx -20\ cm$ to $z \approx -8\ cm$. On the area where the peak of the cut out events is situated the distribution of the events over the y-z-vertex-plane is non-uniform. The number of events increases relatively much in the y-z-area of $\approx 10\ cm < z < \approx 15\ cm$ and $\approx -2\ cm < y < \approx 2\ cm$. This high amount of events in that region is probably caused by annihilations in the veto-counter. Figure 3.4 shows all events that are located within the z-vertex. The z-vertex seems to have a deviation of ≈ 0.55 cm left from the center. This is important and has to be considered in the reconstruction process since a deviation leads to a deviation of the annihilation vertex, as well.

Table 3.2: Statistics that are obtained after the preselection.

Events	Number of events	Share (%)
Total	14875517	100
2 charged events	10037362	≈ 67.68
Positive and negative charge	8791253	≈ 59.10
2-Gamma-events	1258241	≈ 8.46
Events inside energy window	1029024	≈ 6.92
Events inside momentum window	670122	≈ 4.50
Z-vertex cut	654595	≈ 4.40

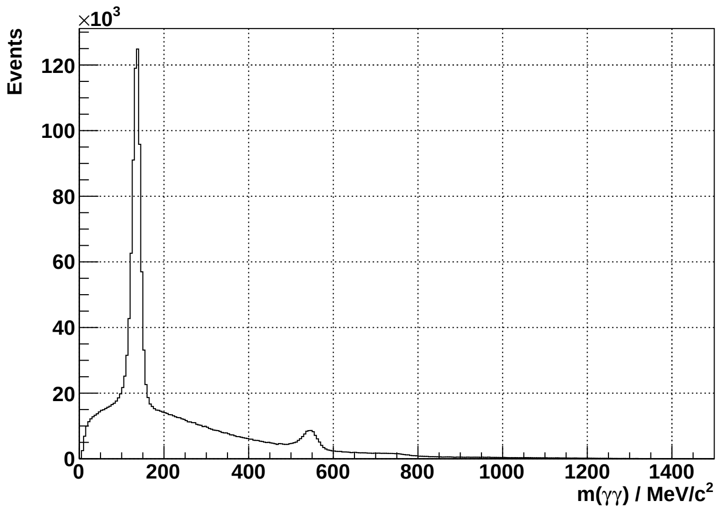

Figure 3.1: The $\gamma\gamma$-spectrum of all events after the preselection. It is still made up by a high share of background.

At the end of this section, before proceeding to the kinematic fit and the background rejection section in general, a deeper look at the η resonance is recommended. Figure 3.5 shows the invariant $\gamma\gamma$-spectrum after the preselection zoomed in between the range 250

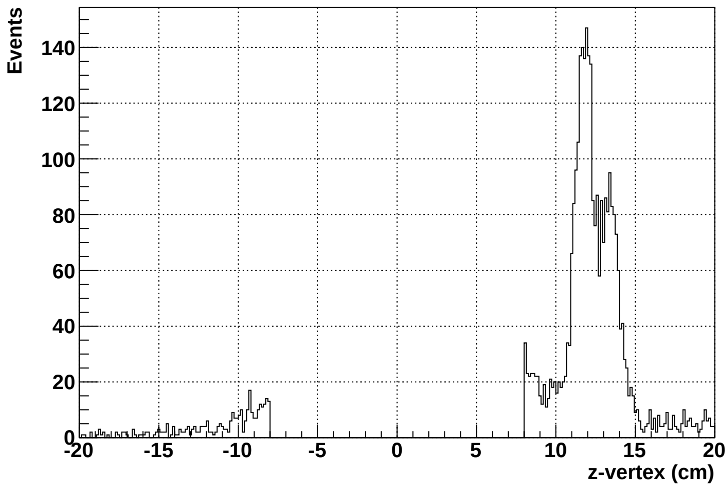

Figure 3.2: The z-vertex. The events depicted are those that are cut out by the z-vertex-cut.

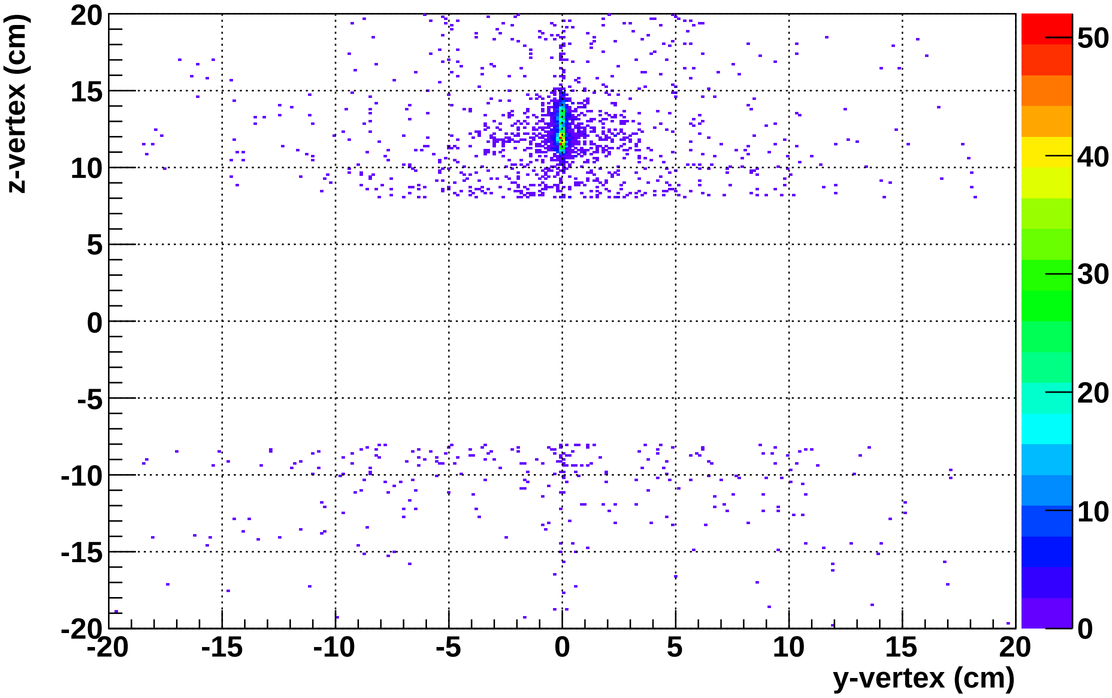

Figure 3.3: Histogramm of the y-z-vertex-plane. It gives an insight on the distribution of the cut-out-events on the y-z-vertex-plane. The events depicted are those that are cut out by the z-vertex-cut.

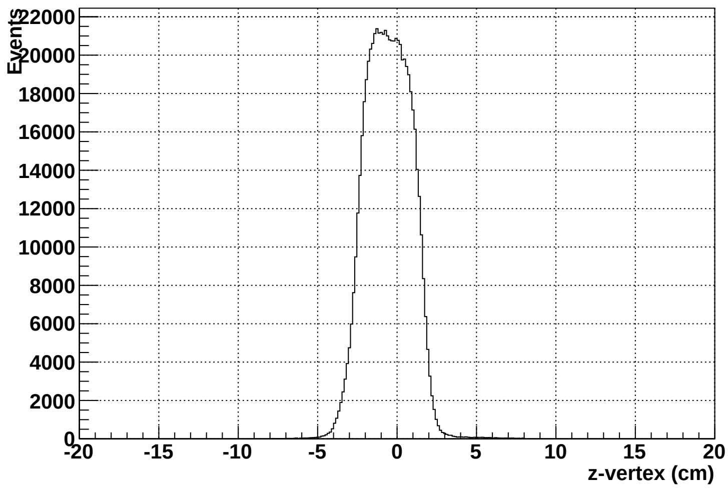

Figure 3.4: Z-vertex distribution. The histogram shows all events that are located within the z-vertex.

MeV up to 750 *MeV*. A resonance is expected to have the shape of a voigtian[2] due to the resolution of the detector. The conclusion from this is that the η-resonance given in figure 3.5 still contains lots of background events. It can be anticipated that in the range of $\approx$ 500 MeV/c^2 downwards and that the tail from $\approx$ 600 MeV/c^2 upwards is sole background. Furthermore it can be anticipated that the η-signal is still contaminated with background events, too. The upcoming section aims to further decrease or even completely separate out background events from signal events.

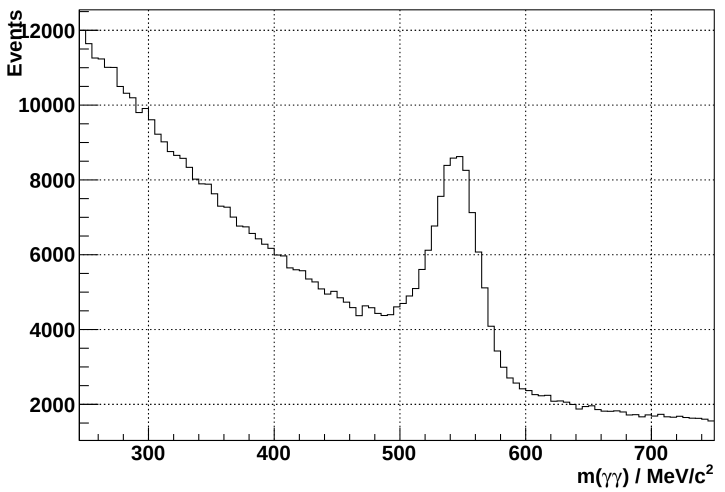

Figure 3.5: The invariant-$\gamma\gamma$ sprectrum in the range between 250 MeV/c^2 - 750 MeV/c^2. The peak is probably an η-resonance.

[2]A voigtian is a convolution of a Gauß-lineshape and a non-relativistic Breit-Wigner-function.

3.4 Background rejection

The background rejection process plays an essential role in the whole analysis. The preselection that was described in the previous section cut out $\approx 96\%$ of the data leaving ≈ 654595 events. The invariant $\gamma\gamma$-spectrum that is depicted in figure 3.1 allows to make the assumption that the majority of the given events are still made up of background events. The goal of this section is to cut out the bulk of it in order be able to proceed to the partial-wave-analysis. Various methods exist in the field of background rejection of which three have been applied and will be presented in this section. The first one will be the kinematic fit that will have probably the greatest effect since it can be expected that most events that are classified as background are non-$\pi^+\pi^-\gamma\gamma$ or non-$\pi^+\pi^-\eta$-final-state events. Those will be cut out mostly by the kinematic fit. After that this section will present some Monte-Carlo studies in order to determine still existent non-$\pi^+\pi^-\gamma\gamma$ and non-$\pi^+\pi^-\eta$-final-state events. The last that will be presented in this section is an event based background rejection method. At that moment only few will make up the remaining data. The applied event based rejection will cut out most of this last remaining background.

3.4.1 Kinematic fit

Theoretical background

The kinematic fit plays an essential role in the analysis of the data. The information on the theory of the kinematic fit can be found in [Pyc2012] and [Kur1995]. The fit makes use of kinematic constraints to improve the data quality. The detector measures various variables for every particle that is detected. These variables are for instance the energy or the azimuth angle of the particle. The method of the kinematic fit makes use of the fact that these variables are bound to constraints like the energy and momentum conservation law and which gives one hypothesis. In total four constraints can be obtained. Other important constraints are the definition of certain decay chains of reaction channels and their intermediate states, respectively. The final state $\pi^+\pi^-\gamma\gamma$, for instance, can be required to have the intermediate state $\pi^+\pi^-\eta$ with $\eta \to \gamma\gamma$. In order to determine whether the hypothesis is fulfilled it is necessary to calculate the invariant mass of the final state system. This can be done with equation 3.1 where m_n denotes the invariant mass of the particle-system, E_i the energy of particle i, $\vec{p_i}$ the three-omentum vector of particle i and n the number of constraints.

$$m_n^2 = \left(\sum_{i=1}^{n} \frac{E_i}{c^2}\right)^2 - \left(\sum_{i=1}^{n} \frac{\vec{p_i}}{c}\right)^2 \tag{3.1}$$

procedure for determining the corrections δy_i for the measured variables y_i is to find the variable $z_i = y_i + \delta y_i$ that fulfills the n constraints

$$f_j(z) = 0 \tag{3.2}$$

where j is the j-th constraint. The determination of the best value can be done with various fit methods. The method that is used by CBKFIT is the χ^2-method. In the χ^2-method the optimum is achieved if the χ^2-function given in equation 3.3 reaches its minimum. The variable C_y in equation 3.3 denotes the covariance matrix of the specific event which becomes the error σ_i if the measurements are uncorrelated. Then equation 3.3 reduces to equation 3.4

$$\chi^2 = \sum_i \sum_j \delta y_i (C_y^{-1})_{i,j} \delta y_j \tag{3.3}$$

$$\chi^2 = \sum_i \left(\frac{\delta y_i}{\sigma}\right)^2 \tag{3.4}$$

Equation 3.4 basically says that the χ^2-value is the quadratic sum of the correction multiplicated by their weight given by the reciprocal of the error. The method that is used to obtain the minimum of the χ^2-function is the method of the lagrange multipliers. The differential equation is given in equation 3.5 where the boundary conditions are contained in the multipiers α_j and k denotes the number of measurements.

$$\frac{\partial \chi^2}{\partial \delta y_i} + \sum_j \alpha_j \frac{\partial f_i}{\partial \delta y_i} = 0 \qquad i = 1, ..., k \tag{3.5}$$

After solving the differential equation system and obtaining the χ^2-value it can be proceeded to determine the confidence-level-distribution $CL(\chi^2)$ which is given in equation 3.6. The CL is a value that can be interpreted as the quality of the fit. Basically, it is the probability that the given event can be described by the set hypothesis. The variable n in equation 3.6 denotes the number of degrees of freedom. A good fit results in a flat CL-distribution.

$$CL(\chi^2) = \int_{\chi^2}^{\infty} \frac{Z^{\frac{n}{2-1}} \exp^{-\frac{z}{2}}}{2^{\frac{n}{2}}\Gamma(\frac{n}{2})} dz \tag{3.6}$$

Another value that gives a measure for the quality of the fit is the pull, which is the normalized deviation of a measured value to the measurement error. An ideal pull distribution is a Gaussian with width $\sigma = 1$ and mean $\mu = 0$.

Applying the kinematic fit

Prior to the kinematic fit the exact errors of the measured values have to be determined. Furthermore the scaling factors for the measurement errors are determined, as well. For the photons the values considered in the kinematic fit are the following:

- The polar angle Θ
- The azimutal angle Φ
- The squareroot of the energy $\sqrt{E}$

The tracks of the charged pions however are being set by the parameters that were described in chapter 2. These were the following:

- The curvature of the helix α
- The angle between the x-axis and the rΦ-projection Ψ_0
- The angle of inclination $tan\lambda$

In order to determine the right errors it is necessary to optimize the pull distributions iteratively by comparing the current pull distribution with the ideal Gaussian-distribution that has a width of 1. The process is repeated until the χ^2 between both distributions reaches its minimum. As a first step the pull distributions for the hypothesis $\pi^+\pi^-\pi^0$ have been optimized since the statistics for the this channel is higher. This makes the channel $\pi^+\pi^-\pi^0$ more easily to handle. Furthermore it is assumed that the optimization of these pulls lead to better pulls of the $\pi^+\pi^-\eta$ hypothesis, as well. The pull distributions of the $\pi^+\pi^-\pi^0$-hypothesis are depicted in figure 3.6. Figure 3.7 shows the pull distributions for the $\pi^+\pi^-\eta$ hypothesis at a beam momentum of 900 MeV/c and its confidence level. The confidence level distribution gives information about how good the determined errors match. An increase in the slope of the confidence level indicates that the errors are set too small. As can be seen from the figure the confindence level distribution is quite leveled for CL>0.1. The pull distributions mostly can be described by a gaussian-distribution, however the $\sqrt{E}$-pull for the uncharged particles has a deviation of $2.66 \cdot 10^{-1}$ from the center. That deviation isn't caused by wrongly determined error values and therefore can't be altered by changing the error values. This deviation might result from the fact that the $\sqrt{E}$-pull does not exactly follow a Gaussian. It was indicated that the target had a deviation of $z_0 = -0.65\ cm$ in the beamtime of 1996. The z-vertex-distribution which is depicted in figure 3.4 shows a deviation of $\approx 0.55\ cm$ from the center. While this deviation is considered in the determination of the constants, it still might have been caused by another error in the configuration of the detector. After the determination of the kinematic constants the events can undergo the kinematic fit.

The goal of this section is to apply the kinematic fit on the data. The data that is left after the preselection will be kinematically fitted with the software package CBKFIT. Three hypotheses have been tested:

1. hypothesis
   $\pi^+\pi^-\gamma\gamma$

2. hypothesis
   $\pi^+\pi^-\eta$

3. hypothesis
   $\pi^+\pi^-\pi^0$

In order to get a first evaluation of the kinematic fit a look at the pull histograms can be useful. The figure in 3.7 depicts five pull-histograms and the CL-distribution of the $\pi^+\pi^-\eta$-fit. The figures 3.7 a)-c) depict the pulls of uncharged particles for Θ, Φ and $\sqrt{E}$. The pulls in figures 3.7 a) and b) fulfill the values that an ideal pull should have with $\sigma_\phi \approx 1.08 \pm 3 \cdot 10^{-3}$, $\mu_\phi \approx 1.69 \cdot 10^{-4} \pm 3.71 \cdot 10^{-3}$ and $\sigma_\Theta \approx 1.12 \pm 3.15 \cdot 10^{-3}$, $\mu_\Theta \approx -4.89 \cdot 10^{-2} \pm 3.89 \cdot 10^{-3}$. The pull of the kinematic variable $\sqrt{E}$ in figure 3.7 c), however, shows a serious deviation from the ideal value of μ with $\sigma_{\sqrt{E}} \approx 1.05 \pm 3.15 \cdot 10^{-3}$ and $\mu_{\sqrt{E}} \approx 2.66 \cdot 10^{-1} \pm 3.80 \cdot 10^{-3}$. The last two histograms in figure 3.7 depict the pulls for charged particles for the kinematic variables α and Ψ_0. The Ψ_0-pull shows a deviation as in the $\sqrt{E}$-pull of uncharged particles. This might be interconnected. The α-pull for charged particles has nearly ideal values with $\sigma_\alpha \approx 1.09 \pm 3.25 \cdot 10^{-3}$ and $\mu_\alpha \approx -2.35 \cdot 10^{-1} \pm 3.22 \cdot 10^{-3}$. Deviations can be seen in the $\sqrt{E}$ and Ψ_0 pull distributions for the $\pi^+\pi^-\pi^0$-fit in figure 3.6, as well. The $tan\lambda$-pulls for both the $\pi^+\pi^-\eta$ and the $\pi^+\pi^-\pi^0$ are not depicted since they also have nearly ideal values. The deviations of the pulls might be due to an incorrect alignment or calibration of the detector or en error in the reconstruction leading to a systematic error in the analysis. The fact that all other pulls are nearly ideal and that the data in general has a high qualtity assures that the distortions caused by that error will be marginal.

Before considering the CL-distribution of the $\pi^+\pi^-\eta$-fit a look at the CL-distribution of the $\pi^+\pi^-\pi^0$-fit should be taken because it turned out that optimizing the $\pi^+\pi^-\pi^0$-fit leads to a greater impovement in the $\pi^+\pi^-\eta$-fit than optimizing the $\pi^+\pi^-\eta$-fit itself. The CL-distribution for the $\pi^+\pi^-\pi^0$-fit is not evenly distributed. The CL-distribution of the $\pi^+\pi^-\eta$-fit in figure 3.7 d) is evenly distributed from a CL-value of ≈ 0.1 upwards. As a conclusion the cut on the CL will be done at 0.1. All events that with CL< 0.1 will be cut out. This will lead to a further decrease of background.

After applying the kinematic fit the number of events decreases significantly. The statistics are listed in table 3.4. The first kinematic fit - on $\pi^+\pi^-\gamma\gamma$ - leads to a decrease of ≈ 29 % in the number of events with 414650 events. The second fit on the $\pi^+\pi^-\eta$-state leads to a decrease of ≈ 93 % in the number of events with 44395 events left. The vast leap from the first fit to the second comes from the huge amount of pions and the fact that $\pi^+\pi^-\eta$ and $\pi^+\pi^-\pi^0$ have the same final state $\pi^+\pi^-\gamma\gamma$. The particles that originate from $\pi^+\pi^-\pi^0$ get only cut out after the fit of $\pi^+\pi^-\eta$. The result of the $\pi^+\pi^-\gamma\gamma$ hypothesis can be seen in the invariant $\gamma\gamma$-mass spectrum in figure 3.8. The first observation that can be made from figure 3.8 is that it differs greatly from figure 3.1 in respect to the background. The background between the resonances seems to have gone completely. The resonances of the π and the η resonance have become clear with the expected shape. A third structure that was already visible in figure 3.1 got uncovered. It is located at between $\approx 700\ MeV/c^2$ up to $\approx 850\ MeV/c^2$ and is probably originating from a co-decay of the reaction $\omega \to \pi^0\gamma$ or $\rho \to \pi^0\gamma$ where a low energetic γ gets lost.

Although the spectrum seems to be free of any background it is worth to zoom in between a shorter range. Since the η, as already told, has a prominent role in this work figure 3.9 depicts the range around the η resonance. The solid line in that figure belongs to the background lineshape that was fitted to the spectrum. The parameters of the fit are given in table 3.3. The value of the parameter $\mu \approx 550\ MeV/c^2$ corresponds to the value of the η-mass with $m_\eta \approx 547.85\ MeV/c^2$. Having examined the resonance the focus should be directed on the bottom areas left and right from the resonance. These areas left and right are still filled with background events which indicates that the resonance itself is still impaired with background events.

3.4.2 Event based background rejection

In addition to the kinematic fit there are other methods to further separate background events from signal events. The method that will be used to further decrease the back-

Table 3.3: The parameters of the fit function of the η-resonance given in figure 3.9. The obtained μ-parameter of the fit, which corresponds to the η-mass, differs by only 0.02 MeV/c^2.

Fit parameters of the peak	Measured result	PDG-value for the η mass
μ **in** MeV/c^2	$\approx 547.87 \pm 0.07$	≈ 547.85

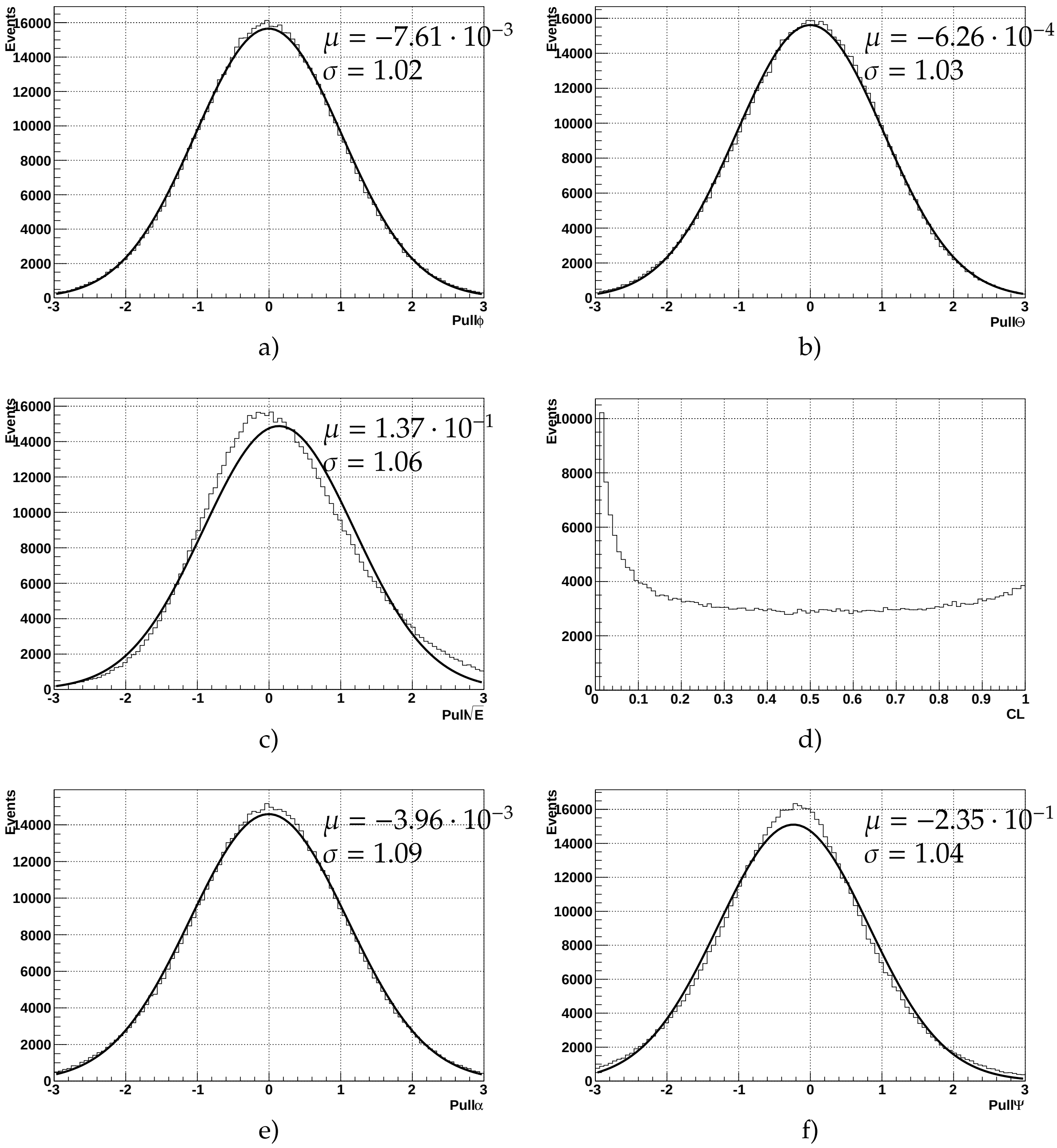

Figure 3.6: The figures in a)-c) show the pull distributions for uncharged particles in the $\pi^+\pi^-\pi^0$-fit. The distributions in a) and b) have nearly an ideal Gauß-shape. Like in the $\pi^+\pi^-\eta$-fit the Pull in c) has a deviation in μ as well. Figure d) shows the confidence-level distribution. The last two histograms e) and f) depict the α and Ψ_0 pull distributions for charged particles.

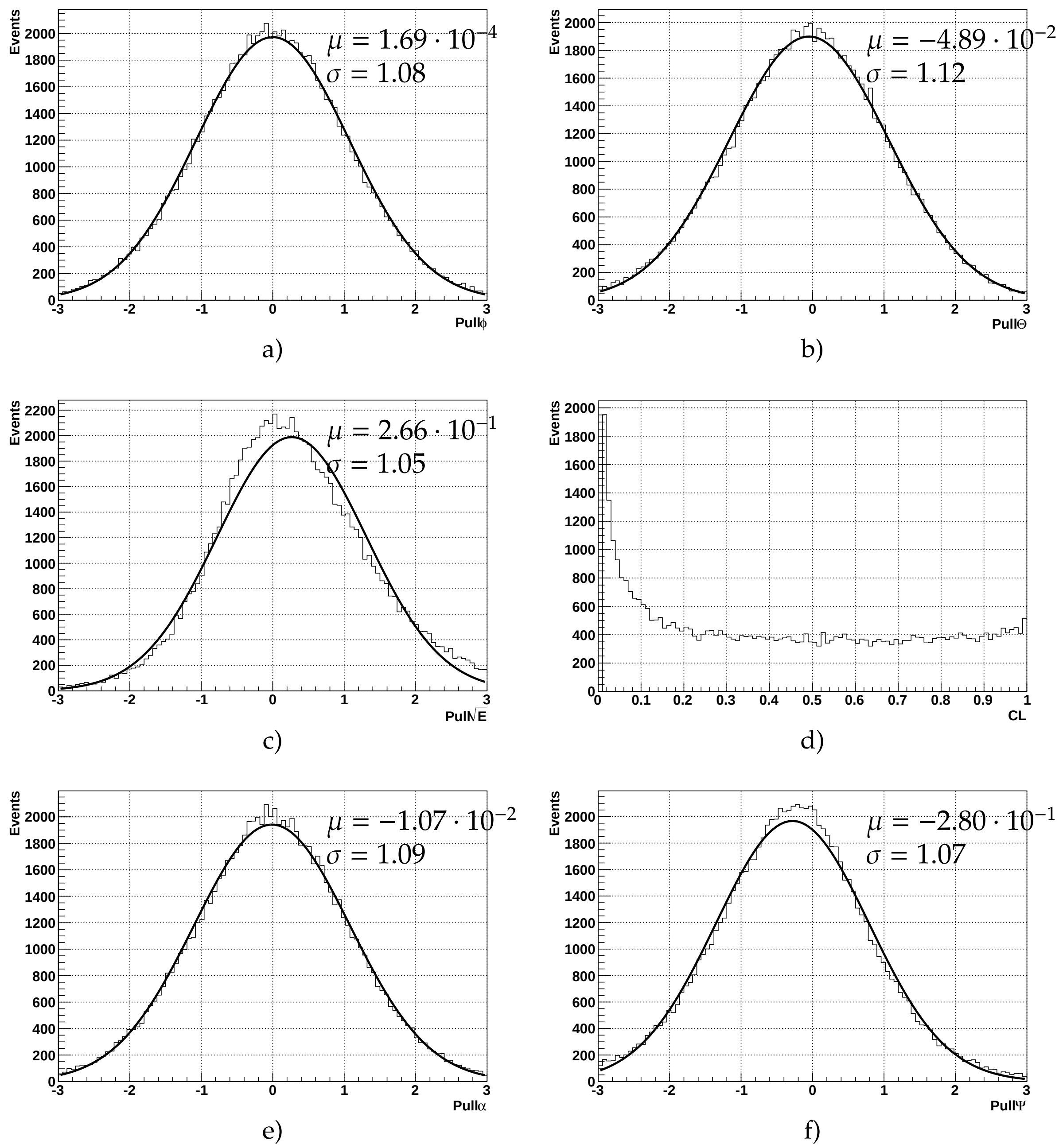

Figure 3.7: The figures in a)-c) show the pull distributions for uncharged particles in the $\pi^+\pi^-\eta$-fit. The distributions in a) and b) have nearly an ideal Gauß-shape. Pull c) has a deviation in μ. Figure d) shows the confidence-level distribution. The last two histograms e) and f) depict the α and Ψ_0 pull distributions for the charged particles.

Table 3.4: Statistics obtained after the kinematic fit.

Events	Number of events	Share (%)
$\pi^+\pi^-\gamma\gamma$	414650	≈ 61.88
$\pi^+\pi^-\eta$	44395	≈ 6.62

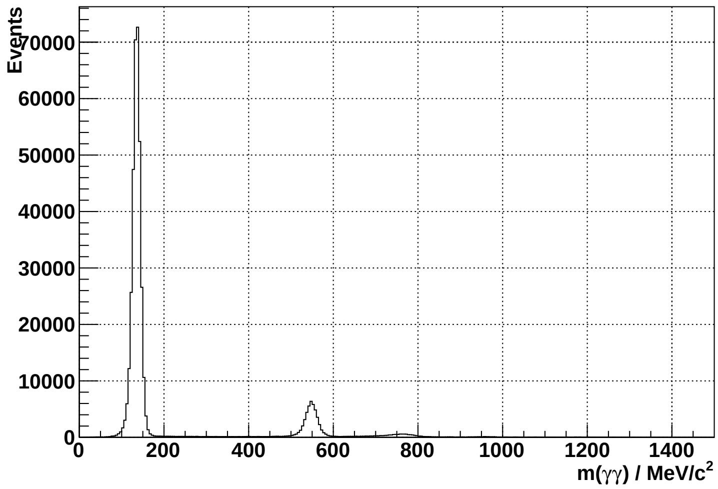

Figure 3.8: The invariant $\gamma\gamma$-mass spectrum after the kinematic fit for the $\pi^+\pi - \gamma\gamma$ hypothesis. Two resonances can be seen from left to right which correspond to π and η.

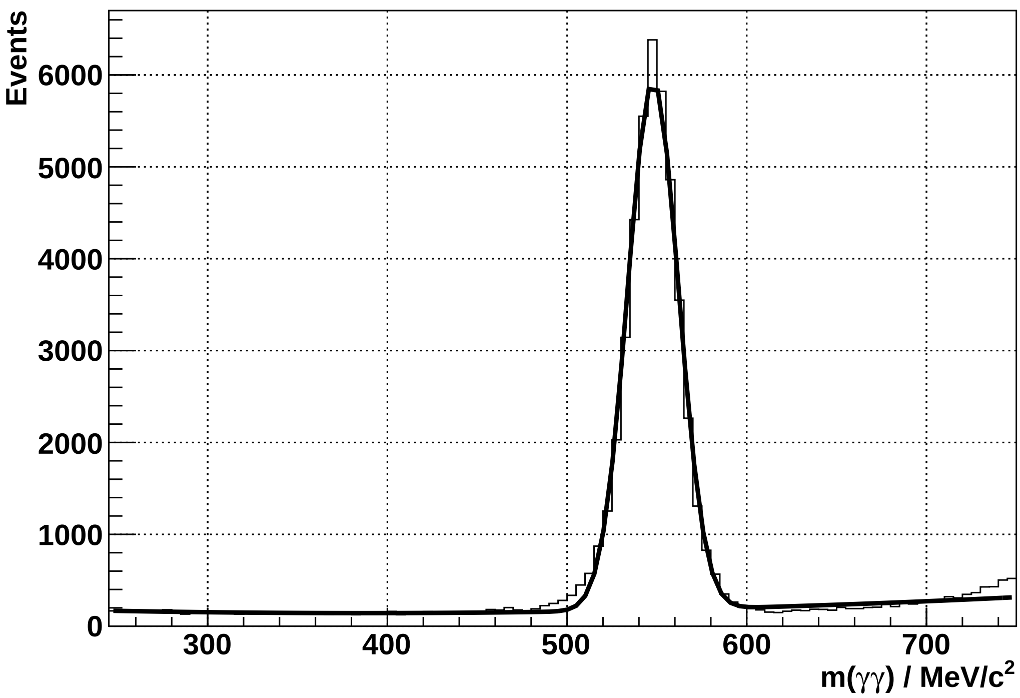

Figure 3.9: The invariant $\gamma\gamma$-mass spectrum after the kinematic fit for the $\pi^+\pi - \gamma\gamma$ hypothesis in the range of 240 MeV/c^2 up to 750 MeV/c^2 after the kinematic fit. The solid line is the graph of the fit function which has the parameters given in table 3.3.

ground is a multivariate subtraction method described in detail in [WIL2009]. The special characteristic of this method is that it separates background events under the η signal shown in figure 3.9. Such a separation is not possible with the kinematic fit introduced in the previous section. That method assigns a probability to each event which is called the Q-factor. The Q-factor gives the probability for an event originating from the signal. As a first step, in order to determine the Q-factor, the distances between the n_c nearest events for every event have to be determined. The value for the n_c nearest events is set to 200 in this thesis. To do this a proper definition of the distance between two events must be given. Furthermore a coordinate system for that metric has to be defined. The definition for the distance between every given event is given in equation 3.7 where the space is spanned by $\vec{\xi}$ and the metric is defined by $\frac{\delta_{kl}}{\sigma_k^2}$ with σ_k the normalization factor and $\delta_{kl} = \xi_k^i - \xi_r^j$.

$$d_{i,j}^2 = \sum_{k \neq r} \left[\frac{\xi_k^i - \xi_r^j}{\sigma_k} \right]^2 \tag{3.7}$$

The phasespace is spanned by the coordinate-system given in equation 3.8.

$$\vec{\xi} = (cos\Theta_{\eta,p}, cos\Theta_{\pi^+\pi^-,p}, \Phi_{\pi^+\pi^-,d}, cos\Theta_{\pi^+\eta,p}, \Phi_{\pi^+\eta,d}) \tag{3.8}$$

The method will be applied on the η-signal of the reaction channel $\bar{p}p \rightarrow \pi^+\pi^-\eta$. Using the η-mass as the reference coordinate $\sigma_{cos\Theta} = 2$ and $\sigma_\Phi = \pi$ the following distance is obtained:

$$\begin{aligned} d_{i,j}^2 = \frac{1}{2^2} \Big[&(\cos\Theta_{\eta,p,i} - \cos\Theta_{\eta,p,j})^2 + (\cos\Theta_{\pi^+\pi^-,p,i} - \cos\Theta_{\pi^+\pi^-,p,j})^2 + \\ &(\cos\Theta_{\pi^+\eta,d,i} - \cos\Theta_{\pi^+\eta,d,j})^2 \Big] + \frac{(\Phi_{\pi^+\pi^-,d,i} - \Phi_{\pi^+\pi^-,d,j})^2}{\pi^2} \\ &+ \frac{(\Phi_{\pi^+\eta,d,i} - \Phi_{\pi^+\eta,d,j})^2}{\pi^2} \end{aligned} \tag{3.9}$$

The functional dependence of the signal and the background on the reference coordinate, m_η, is

$$S(m_i, \vec{\xi}_i) = F(m_{\pi^+\pi^-\eta}) \cdot V(m_i, m_\eta, \Gamma_\eta, \sigma) \approx A \cdot V(m_i, m_\eta, \sigma, \Gamma_\eta) \tag{3.10}$$

$$B(m_i, \vec{\xi}_i) = B(m_i, \vec{\xi}_{\pi^+\pi^-\eta}) \approx a \cdot m_i + b \cdot m_i^2 + c \tag{3.11}$$

where $m_\eta = 547.853\,MeV/c^2, \Gamma_\eta = 1.30\,MeV, \sigma$ is the resolution of the detector, $\vec{\alpha} = (s, b_1, b_0)$ obtained from the fit and

$$V(m_{\pi^+\pi^-\eta}, m_\eta, \Gamma_\eta, \sigma) = \frac{1}{\sqrt{2\pi}\sigma} Re\left[w(\frac{1}{2\sqrt{\sigma}}(m_{\pi^+\pi^-\eta} - m_\eta) + i\frac{\Gamma_\eta}{2\sqrt{2}\sigma}) \right] \tag{3.12}$$

the Voigtian with the complex error function w. The Voigtan is a convolution of a Gaussian and the non-relativistic Breit-Wigner function taking the resolution of the detector into account. It should be noted that in [WIL2009] the background is assumed to be linear of the form $B(m_i, \vec{\xi}_i) = B(m_i, \vec{\xi}_{\pi^+\pi^-\eta}) \approx a \cdot m_i + b$. In this analysis a polynomial of second order proved to fit better on the background. The mass-spectrum is fitted with the sum of 3.10 and 3.11 using the maximum-likelihood-method. The Q-Factor is then obtained by

$$Q = \frac{S}{S+B} \tag{3.13}$$

As an example the Q-factor for one event of the η-siganl is depicted in figure 3.10 with an mass offset of 400 MeV/c^2.

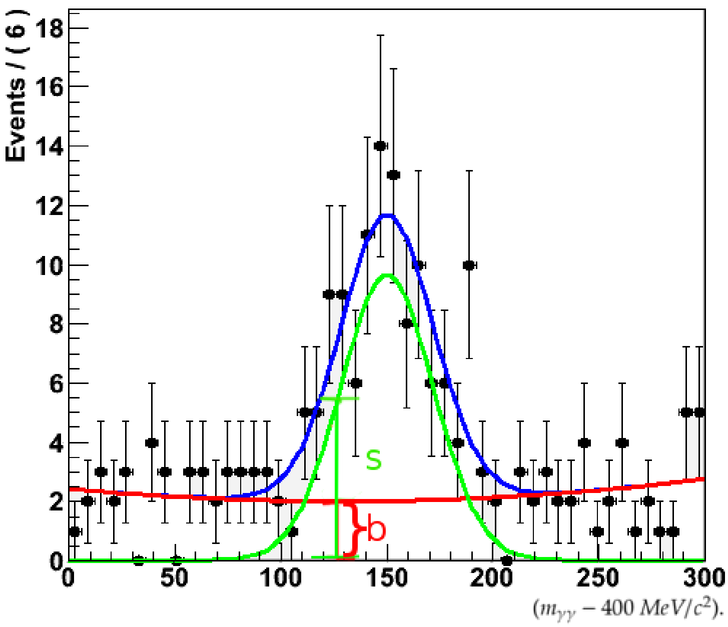

Figure 3.10: As an example the Q-factor for one event for the η signal - all events (blue), only signal events (green) and background events (red) with $Q = \frac{S}{S+B}$. The x-axis has an offset and is given by $(m_{\gamma\gamma} - 400\,MeV/c^2)$.

3.5 Results

Applying the event based background rejection method on all events results in Figure 3.11. It depicts the signal events (blue) which have been weighted with the Q-factor, the background events (red) weighted with $1 - Q$ and the unweighted events (black). The graph of the background events has a nearly linear course as expected. Especially the outer regions from 400 MeV/c^2 to $\approx$ 500 MeV/c^2 and from $\approx$ 600 MeV/c^2 to 700 MeV/c^2 which are expected to be made of solely background match exactly with the graph of the $1 - Q$-weighted events.

The Figures 3.12 and 3.13 depict the Dalitz-plot for the Q-weighted signal events and the Dalitz plot for the events with weight 1-Q, respectively (more information on Dalitz plots in appendix A). The various resonances in the signal Dalitz plot will be discussed later. The background Dalitz plot shows high background in regions of resonances in the signal Dalitz plot. Comparing these regions of the background with the Q-weighted signal dalitz plot some structures seem to be similiar.

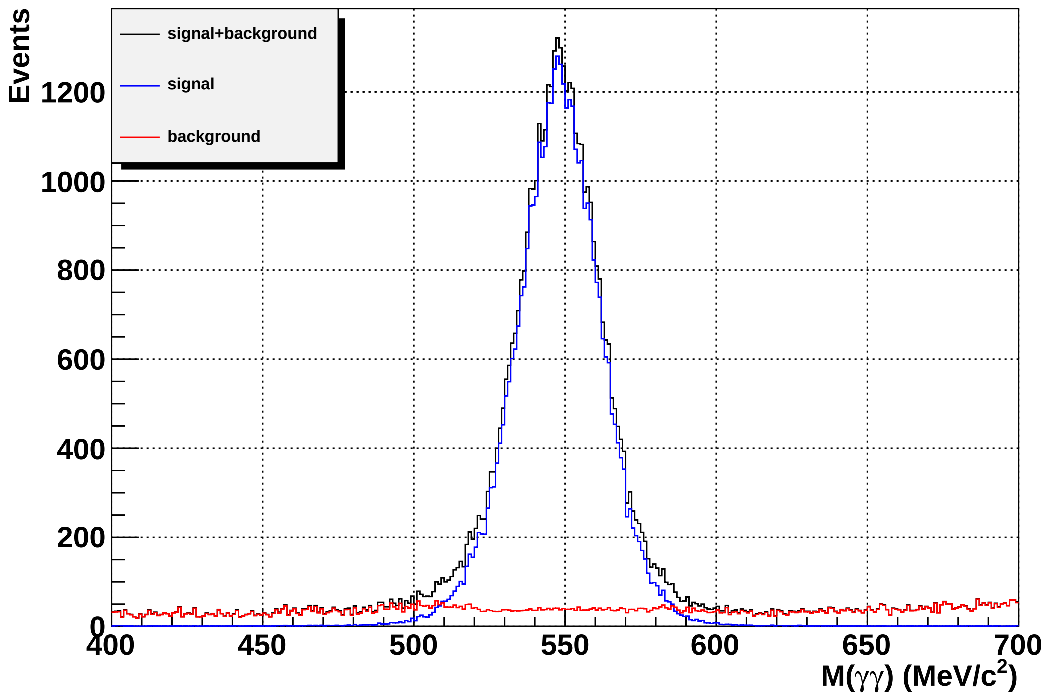

Figure 3.11: The invariant-$\gamma\gamma$-mass spectrum after the kinematic fit for the $\pi^+\pi - \gamma\gamma$ hypothesis for the η-resonance for all events (black), only Q-weighted events (blue) and $1 - Q$-weighted events (red).

First assumptions about intermediate states can be made with the help of the invariant mass spectra of the $\pi^+\pi^-$-system and the $\pi^+\eta$ which are depicted in figures 3.14 and 3.15 respectively. Two clearly visible resonances can be seen in figure 3.14. The first one lies in

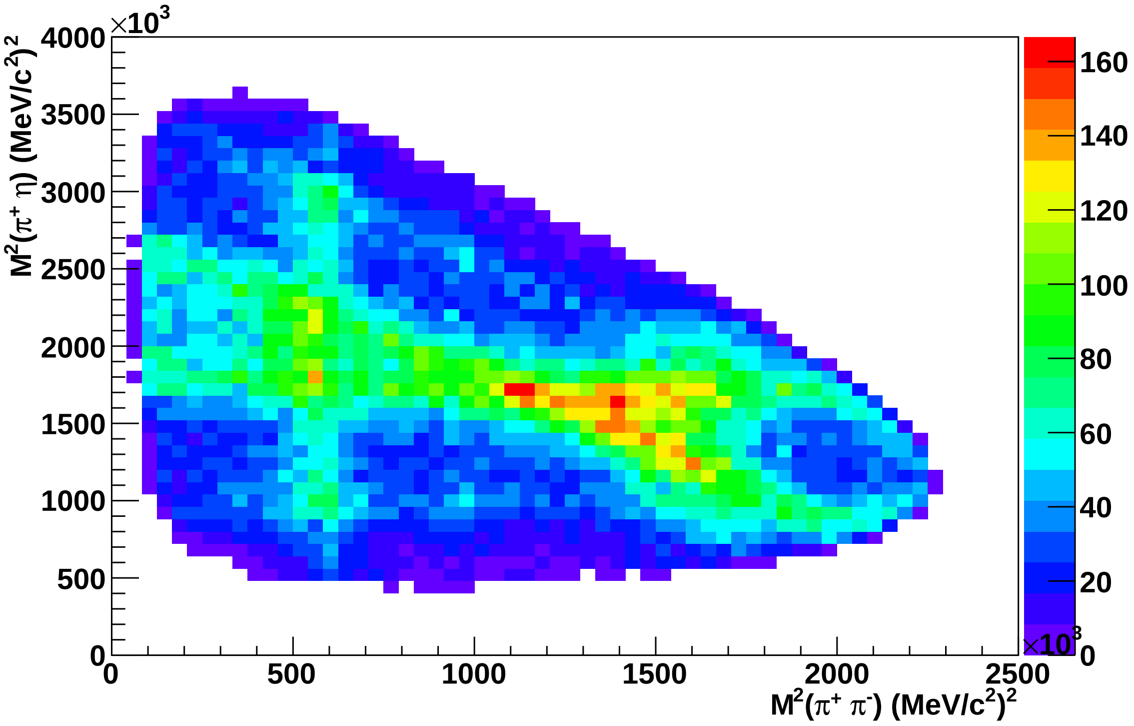

Figure 3.12: The signal Dalitz plot with the Q-weighted data events. Various resonances can be seen like the ρ-resonance, the $a_0(980)$, $f_0(980)$, $f_2(1270)$ and $a_2(1320)$ giving a starting point for the partial wave analysis in the next chapter.

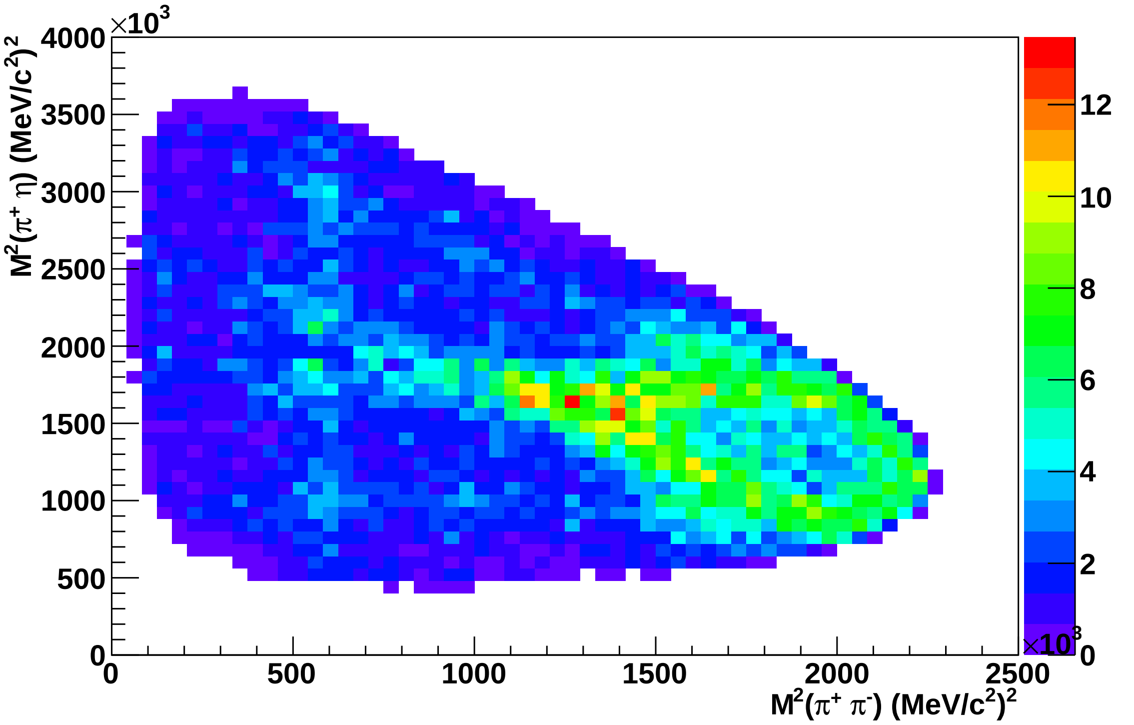

Figure 3.13: The background dalitz plot with the $1 - Q$-weighted data events. Some structures seem to be similiar to the Q-weighted dalitz plot.

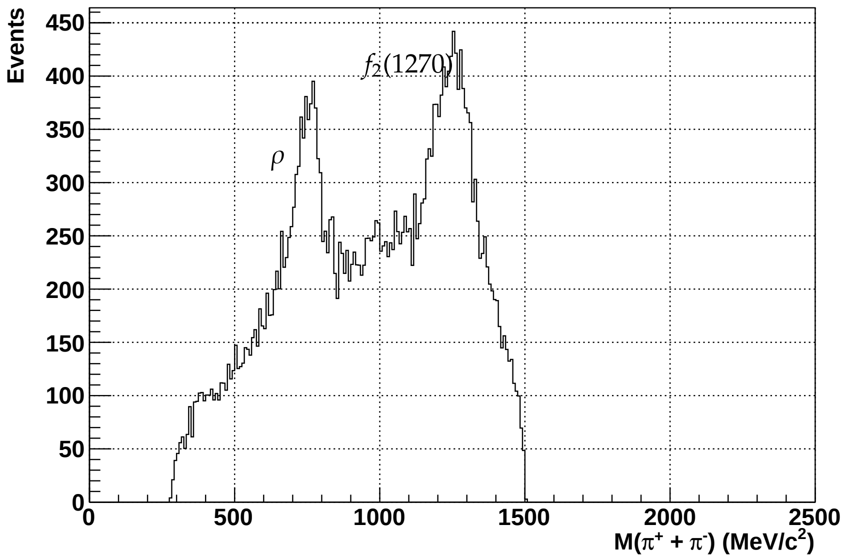

Figure 3.14: Invariant $\pi^+\pi^-$-mass spectrum after the event based background rejection.

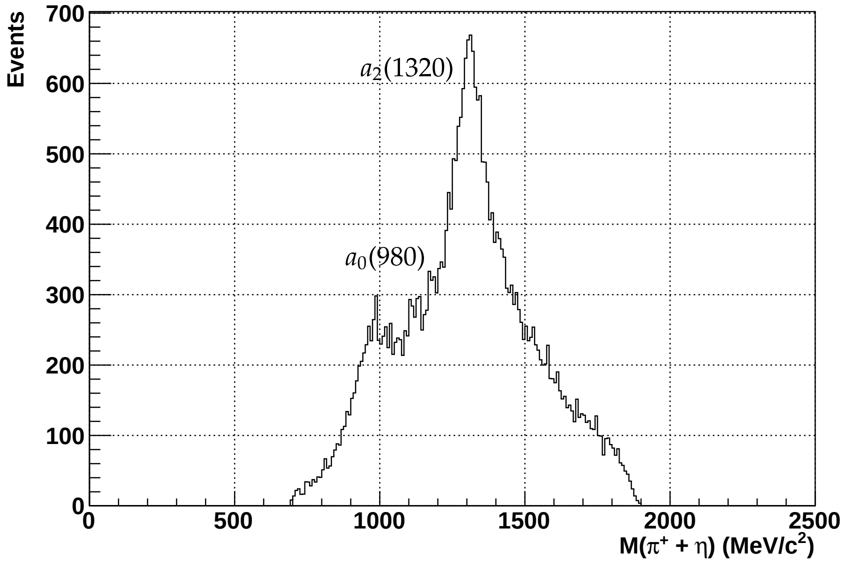

Figure 3.15: Invariant $\pi^+\eta$-mass spectrum after the event based background rejection.

the area between $\approx 650\ MeV/c^2$ up to $\approx 800\ MeV/c^2$ which can be said to be the ρ-meson since it corresponds to its mass with $m_\rho \approx 770\ MeV/c^2$. The second resonance is probably a $f_2(1270)$ and ranges from $\approx 1100\ MeV/c^2$ to $\approx 1350\ MeV/c^2$. A more detailed look at that spectrum reveals a step-like shape within the range from $\approx 450\ MeV/c^2$ to $\approx 500\ MeV/c^2$. The mass spectrum that is depicted in figure 3.15 has one dominating resonance within the range from $\approx 1200\ MeV/c^2$ to $\approx 1500\ MeV/c^2$ which corresponds to the $a_2(1320)$-mass with $m_{a_2(1320)} \approx 1318\ MeV/c^2$. The smaller peak between the range $\approx 900\ MeV/c^2$ up to $\approx 1000\ MeV/c^2$ belongs to the $a_0(980)$ with a mass of $m_{a_0(980)} \approx 980\ MeV/c^2$.

3.6 Monte carlo studies

Monte carlo studies can help to identify states that could mistakenly be taken as the $\pi^+\pi^-\eta$-state. This can happen if one or more particles get lost. For example if one η in the $\pi^+\pi^-\eta\eta$-state gets lost in some way this will result in such a scenario. The relevant decay channels are simulated with Monte Carlo generated events. The software that is used is CBGEANT. Table 3.5 shows the statistics for the Monte Carlo events for the $\pi^+\pi^-\eta$-state after the kinematic fit. $\approx 40\%$ of the events are filtered out after the fit on $\pi^+\pi^-\gamma\gamma$ which is $\approx 20\%$ more than the amount cut out from the data events. This is an indication that other reaction channels with the final state $\pi^+\pi^-\gamma\gamma$ have a considerable share on the data events. The fit on $\pi^+\pi^-\eta$ decreases the amount of Monte Carlo events by only $\approx 2\%$ which corresponds to the expectations since the Monte Carlo events were generated only for the $\pi^+\pi^-\eta$-state.

Table 3.5: Statistics obtained after the kinematic fit for Monte Carlo events for the decay $\pi^+\pi^-\eta \to \pi^+\pi^-(\gamma\gamma)$.

Events	Number of generated events	Share (%)
Total	10000000	≈ 100
After preselection	6176665	≈ 61.77
$\pi^+\pi^-\gamma\gamma$	3076794	≈ 30.77
$\pi^+\pi^-\eta$	2982402	≈ 29.82

Monte Carlo events on various reaction channels were generated in order to find out how much events that are misidentified as $\pi^+\pi^-\eta$-events could possibly pass the kinemtatic fit. The relevant channels that were simulated are listed in Table 3.6. The table shows the total amount of events after the preselection of the considered channels. The total amount for all channels 1000000. The results show that the events of the channels $\pi^+\pi^-\eta\eta$, $\pi^+\pi^-\eta\eta\pi^0$ and $\pi^+\pi^-\eta\pi^0\pi^0$ got completely cut out or at most 1 event passed. The channel $\pi^+\pi^-\pi^0$ has only $\approx 2.5 \cdot 10^{-5}$ of all events left which is negligible, too. Only channel $\pi^+\pi^-\pi^0\pi^0$ has a share events that passed the $\pi^+\pi^-\eta$-fit with 430 events. However, the ratio is still

Table 3.6: Statistics obtained after the kinematic fit for Monte Carlo events of various reaction channels.

Fit	**Total**	$\pi^+\pi^-\gamma\gamma$	Share	$\pi^+\pi^-\eta$	Share
$\pi^+\pi^-\eta\eta$	1000000	41	$\approx 4.1 \cdot 10^5$	1	$\approx 0\%$
$\pi^+\pi^-\eta\eta\pi^0$	1000000	0	0%	0	0%
$\pi^+\pi^-\eta\pi^0\pi^0$	1000000	0	0%	0	0%
$\pi^+\pi^-\pi^0$	1000000	215496	≈ 0.22	25	$\approx 2.5 \cdot 10^{-5}$
$\pi^+\pi^-\eta\pi^0$	1000000	669	$\approx 6.69 \cdot 10^{-4}$	96	$\approx 9.6 \cdot 10^{-5}$
$\pi^+\pi^-\pi^0\pi^0$	1000000	5394	≈ 5.39	430	$\approx 4.3 \cdot 10^{-4}$

relatively small which leads to the conclusion that a contamination of the data with events from these channels are negligible. A cut on any of these channels would therefore cut out more signal events than events originating from these states. This led to the decision not to do a veto cut on these channels.

3.6.1 Detector efficiency

The detection efficency and reconstruction efficency vary over the measured momentum and energy ranges. As a consequence each monte carlo generated event that will be used in the partial wave analysis is muliplicated with its detection and reconstruction efficency ϵ_i. In order to determine the reconstruction efficencies Monte Carlo events are generated for the final state $\pi^+\pi^-\eta$. The number of generated Monte Carlo events is $\approx 1 \cdot 10^7$. The events are then subjected to all background rejection methods and cuts that were described previously in this chapter. Because of the varying efficency the Monte Carlo events, which are generated phasespace distributed events, are thus not homogenously distributed in the dalitz plot as can be seen in figure 3.16. The efficency seems to be equally distributed over the momentum range but areas with higher efficencies then the overall average exist.

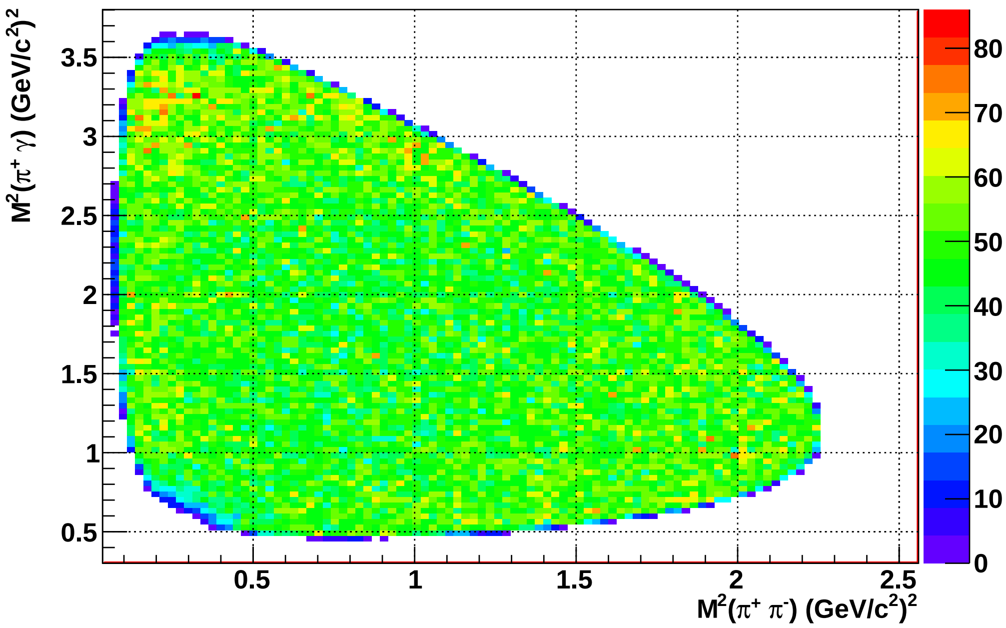

Figure 3.16: Dalitz plot visualizing the detector efficiency.

4 The partial wave analysis

This chapter is aimed at deriving the formalism and explaining the theoretical background of the partial wave analysis. As already told the dalitz plots show special structures, for example resonances. In order to identify the contributing resonances in the $\pi^+\pi^-\eta$-data it is necessary to do a partial wave analysis. The formalism that will be applied here is the helicity formalism. After describing the helicity formalism the isobar model will be introduced. The isobar model reduces a three-body problem down to a two-body problem. The technical realisation of the partial wave analysis and the log-likelihood method are presented in this section as well.

4.1 Helicity formalism

The partial wave analysis requires the determination of the various angular distributions. One preferred method for the determination of the angular distributions is the helicity formalism which allows an uniform handling of both mass and massless particles. The helicity operator is invariant over rotations. However, it is not invariant over boosts along $\overline{p}$. This section covers amongst other things the rotation of angular momenta, helicity states and the transition amplitudes. The helicity formalism is comprehensively covered in [Ric84].

4.1.1 Definition of helicity

The helicity λ is defined as the projection of the spin onto the momentum of a particle. Mathematically it is given as

$$\lambda = \pm \vec{S} \cdot \hat{p} \tag{4.1}$$

where $\vec{S}$ is the spin vector and $\hat{p} = \frac{\vec{p}}{|\vec{p}|}$. λ can also be written as a function of total angular momentum J given in equation 4.2. This is possible since the angular momentum vector $\vec{l}$

is vertical to the direction of the momentum vector $\vec{p}$ and hence the scalar product of the two is $\vec{l} \cdot \vec{p} = 0$.

$$\lambda = \pm\vec{J} \cdot \hat{p} \tag{4.2}$$

The λ is with the z-component of the spin given as

$$\lambda = \pm s_z \cdot \hat{p} \tag{4.3}$$

and since the s_z-component of the spin has 2s+1 possible configurations with values $s_z = -|s|, -|s-1|, ..., |s-1|, |s|$ the third component of the helicity λ, as well, has 2s+1 possible configurations. The values of λ can be $\lambda = -|\lambda|, -|\lambda - 1|, ..., |\lambda - 1|, |\lambda|$. The total helicity of a two particle system in which both particles have the same mother particle is given in equation 4.4.

$$\lambda = \lambda_1 - \lambda_2 \tag{4.4}$$

Equation 4.4 follows from the fact that the momentum vectors of the two particles have the same absolute value with opposite directions (equation 4.5).

$$\vec{p_1} = -\vec{p_2} \tag{4.5}$$

4.1.2 Rotation of angular momentum states

A particle that has a total angular momentum of J and z-component m is seen in the state $\left|jm\right\rangle$ by an observer O where $\left|jm\right\rangle$ is the eigenstate of the operators J^2 and J_z. An observer observing the particle at a position that is relative to O rotated by a rotation $r(\alpha, \beta, \gamma)$ sees the particle in the state $\left|j'm'\right\rangle$. The variables α, β, γ are the Euler angles that describe elemental rotations of coordinate systems. The primes denote the different inertial system with S the inertial system of the observer O and S' the intertial system of O'. The two states are connected over the rotation operator $R(r)$ which is a function of the Wigner-D-matrices $D^j_{m',m}$. The Wigner-D-function is defined in equation 4.6.

$$\left\langle jm\right| R(\alpha, \beta, \gamma) \left|j'm'\right\rangle = \delta_{jj'} D(j, m, m', \alpha, \beta, \gamma) \tag{4.6}$$

The rotation operator $R(r)$ can be found to be

$$R(\alpha, \beta, \gamma) = e^{-i\alpha J_z} e^{-i\beta J_y} e^{-i\gamma J_z} \tag{4.7}$$

with J_i the total projection of the angular momentum on the i-axis. The fact that equation 4.6 is non-zero only for $j = j'$ and after substituting 4.7 it becomes

$$D(j, m, m', \alpha, \beta, \gamma) = \langle jm \middle| e^{-i\alpha J_z} e^{-i\beta J_y} e^{-i\gamma J_z} \middle| jm' \rangle \tag{4.8}$$

and since $e^{-i\gamma J_z} \left| jm \right\rangle = e^{-im\gamma} \left| jm \right\rangle$ and $e^{-i\alpha J_z} \left| jm \right\rangle = e^{-im\alpha} \left| jm \right\rangle$ equation 4.8 can further be written as

$$\begin{aligned} D(j, m, m', \alpha, \beta, \gamma) = e^{-im\alpha} \langle jm \middle| e^{-i\beta J_y} \middle| jm' \rangle e^{-im\gamma} = \\ e^{-im\alpha} d(j, m, m', \beta) e^{-im\gamma} \end{aligned} \tag{4.9}$$

with

$$d(j, m, m', \beta) = \langle jm \middle| e^{-i\beta J_y} \middle| jm' \rangle . \tag{4.10}$$

Further information on Wigner-D-matrices can be found for example in [Schul2000].

4.2 The isobar model

In the isobar model the reaction $\bar{p}p \to \pi^+\pi^-\eta$ is considered to consist of processes in which only two mesons are involved. As a consequence the reaction $\bar{p}p \to \pi^+\pi^-\eta$ can be seen as a sequential two-body-decay which has two different reaction types:

1. $\bar{p}p \to X\eta \Longrightarrow X \to \pi^+\pi^-$
2. $\bar{p}p \to X^\pm\pi^\mp \Longrightarrow X^\pm \to \pi^\pm\eta$

In the first reaction type a mother particle decays into the resonance X and η. The resonance X again decays into two daughter particles $\pi^+\pi^-$ and the whole reaction ends up in the state $\pi^+\pi^-\eta$. The figure 4.1 shows as an example the first of the processes listed above with the $\bar{p}p$-annihilation from which the isobar X and an η are created. The η is the recoil particle. The angles Θ and Φ are the production angles of the resonance in the $\bar{p}p$ rest frame, with the antiproton beam lying in the z-axis and with a positive direction.

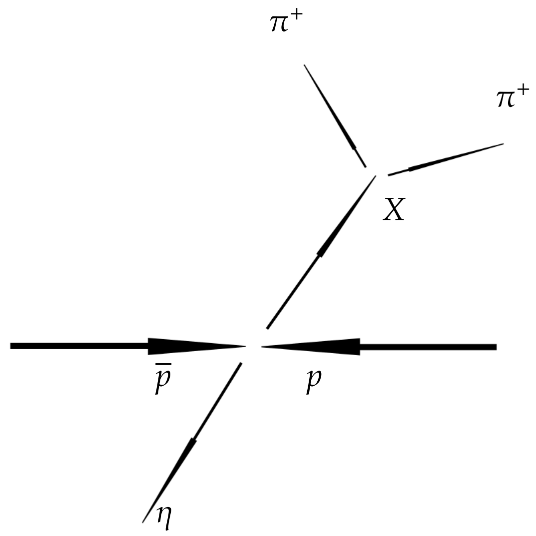

Figure 4.1: Kinematic process of the $\overline{p}p$-annihilation boost in the $\overline{p}p$ rest frame. The direction of the antiproton $\overline{p}$ is set to be in the positive direction of the z-axis.

As a next step the angle between the production plane and the decay plane in the $\overline{p}p$-annihilation rest frame has to be determined. That angle is called the Treiman-Yang angle.

4.2.1 Initial states and the $\overline{p}p$-annihilation in flight

It is possible to determine selection rules for the $\overline{p}p$-reactions. The conservation laws of angular momentum J, charge conjugation C and parity P will be used to derive those rules.

The $\overline{p}p$-reaction can adopt two possible total spin values which are $S_{\overline{p},p} = 0$ and $S_{\overline{p},p} = 1$. This leads to initial states that can be distinguished by the multiplicity $\mu = 2S_{\overline{p},p} + 1$ with $\mu_1 = 0$, which denotes a singlet state, and $\mu_2 = 3$, which denotes a triplet state. The initial states can be obtained with the angular momentum $L_{\overline{p},p} = 0, 1, 2, ...$, the P-parity and the C-Parity. The possible values for a triplet-state are given by the equations **??**-**??**. Due to quantum number conservation the final states of the $^{2S+1}L_j$ initial state can adopt only specific quantum numbers given in table 4.1. A conclusion from the possible quantum number values in table 4.1 is that final states with quantum numbers $J^{PC} = 0^{--}, 0^{+-}, 1^{-+}, 2^{+-}, ...$ are not possible. However, it should be noted that the $\pi\eta$-final state possibly leading to the $\pi_1(1400)$ can have a quantum number configuration of 1^{-+}.

The $\overline{p}p$-annihilation is a complex process in which the quarks have to considered for a proper understanding as well. An encounter of a proton's quark with an antiproton's antiquark leads to a rearrangement of the remaining quarks into mesons.

Table 4.1: Possible initial states of the $\bar{p}p$-system with spin singlet states and spin triplet states mixed.

J	Singlet $\lambda = 0$	J^{PC}	Triplet $\lambda = \pm 1$	J^{PC}	Triplet $\lambda = \pm 1, 0$	J^{PC}
0	$^1S_0$	0^{-+}			$^3P_0$	0^{++}
1	$^1P_1$	1^{+-}	$^3P_1$	1^{++}	$^3S_1, ^3D_1$	1^{--}
2	$^1D_2$	2^{-+}	$^3D_2$	2^{--}	$^3P_2, ^3F_2$	2^{++}
3	$^1F_3$	3^{+-}	$^3F_3$	3^{++}	$^3D_3, ^3G_3$	3^{--}
4	$^1G_4$	4^{-+}	$^3G_4$	4^{--}	$^3F_4, ^3H_4$	4^{++}
5	$^1H_5$	5^{+-}	$^3H_5$	5^{++}	$^3G_5, ^3I_5$	5^{--}
6	$^1I_6$	6^{-+}	$^3I_6$	6^{--}	$^3H_6, ^3J_6$	6^{++}

What can be said about the isospin states of the $\bar{p}p$-system is that they are a composition of $|00\rangle$ and $|10\rangle$ given in equation 4.11. The values i_1 and i_2 denote the mixing ratios of both states with the constraint $i_0^2 + i_1^2 = 1$.

$$|\rangle = i_0\,|00\rangle + i_1\,|10\rangle \tag{4.11}$$

4.3 Log-likelihood-method

The amount of events decreases drastically after applying background reduction methods, whereas the χ^2-method, that was introduced in the section of the kinematic fit earlier, requires a high amount of statistics. Instead an event based fitting method is the method of choice. In this work it will be the log-likelihood-method which assigns a probabilty based on the fitted model to each event. This probability gives a fit quality.

The likelihood function is obtained by multiplicating the probabilities. The probability for one event p_i to be detected is given by

$$p_i = C \cdot w_i \epsilon_i. \tag{4.12}$$

The probability is a function of w_i and ϵ_i. The variable ϵ_i is the detector and reconstruction efficiency and w_i the total amplitude squared. The constant C is given as 1 divided by the integral over the whole phasespace (4.13).

$$C = \left(\int (w\epsilon)d\Omega\right)^{-1} \tag{4.13}$$

Hence the likelihood-function is given by

$$L(\vec{p}) = N! \prod_{i=1}^{N} p_i \tag{4.14}$$

with N the total amount of events. If we substitute 4.12 into equation 4.14 we get

$$L(\vec{p}) = N! \prod_{i=1}^{N} \frac{w_i \cdot \epsilon_i}{(\int (w\epsilon) d\Omega)} \tag{4.15}$$

The integral in the denominator is solved using Monte Carlo integration. Due to technical reasons it is more comfortable to take the logarithms of the likelihood function and to multiplicate the logarithmic likelihood function with -1. That way the product turns into a sum which is easier to handle and the multiplication with -1 has the advantage that minimization algorithms can be used. The NLL (negative logarithmic likelihood function) is then given by

$$NLL = -ln(L) \tag{4.16}$$

with L the likelihood function. Substituting L into equation 4.17 gives

$$NLL = -ln(N!) - (\sum_{i=1}^{N} ln(w_i) + \sum_{i=1}^{N} ln(\epsilon_i)) + ln(\Phi) \tag{4.17}$$

where Φ results from the Monte Carlo integration of the denominator in equation 4.15 and is given as

$$\Phi = \frac{\sum_{i=1}^{N_{MC}} ln(w_i)}{N_{MC}}. \tag{4.18}$$

The goal in the fit process is to minimize the NLL-function in order to find the best fit. Prior to the fit some simplifications can be made. The sum over the ϵ_i in equation 4.17 is a constant and can be omitted in the NLL-function. This is because a constant has no effect in comparing the various fit results. Furthermore the first subtrahend $-ln(N!)$ can be approximated with the stirling equation given in 4.19.

$$ln(N!) \approx Nln(N) - N \tag{4.19}$$

After introducing the generalized probability function we obtain from 4.17 the equation 4.20.

$$NLL = -\sum_{i=1}^{N} ln(w_i) + ln(\Phi) + \frac{1}{2} \cdot (\Phi - 1)^2 \tag{4.20}$$

Before applying the NLL-function it is necessary to incude the Q-factor that was determined in the previous chapter for each event. To include the Q-factor the NLL-function needs to be modified and as a result we get equation 4.21.

$$NLL = -\sum_{i=1}^{N_{data}} ln(w_i) \cdot Q_i + \left(\sum_{i=1}^{N_{data}} Q_i\right) \cdot ln(\Phi) + \frac{1}{2}\left(\sum_{i=1}^{N_{data}} Q_i\right) \cdot (\Phi - 1)^2 \tag{4.21}$$

Fitting software

Various software packages are used throughout the whole fitting process. At the very core of all software packages that are needed is *PAWIAN* which is used for the partial wave analysis. It is still under development at the "Institut für Experimentalphysik I" which is located at the Ruhr-Universität in Bochum, Germany. The development of *PAWIAN* is primarily for the $\overline{P}ANDA$-experiment. *PAWIAN* is written in C++ and is an object oriented software framework that can be used for the development of specially tailored partial wave analysis software. The minimization of the NLL-function is done by two different software packages which are the *Minuit*2 and a tool based on generic algorithms. In the minimization process *Geneva* is used first since it uses Monte Carlo methods to start concurrently a huge amount of minimizations at different locations in order to find the area where the global minimum is located. This makes *Geneva* quite fast but unfortunately the results aren't always very precise. At this point the parameters are handed over to *Minuit*2 which is based on the gradient descent method and therefore is more precise than *Geneva*. The analysis is done with ROOT again. Apart from these the software packages qft++ for the determination of the Wigner-D-functions and the Clebsch-Gordon coefficients and the C++ class libraries *Boost* are used.

4.3.1 Determination of the significance of contributing waves and the *AICc* value

As already told it is necessary to set up various hypotheses with distinct contributing waves which are then fit to the data. The fit results in a likelihood-value (see section 4.3.1) which is an information about the quality of the fit. Some of the hypotheses will have better likelihood-values than others which, however, does not have to mean that these hypotheses are better as well. The improvement of the likelihood-function has to be significant. The formalism to determine the significance of an improvement will be introduced in this subsection. It is based on the formalism described in [Schul2012]. Fits that have more free parameters will possibly have smaller and thus better likelihood values L_B compared to the likelihood value L_A. The ratio of these two becomes then

$$0 \leq \Lambda = \frac{L_B}{L_A} \leq 1. \tag{4.22}$$

The likelihood is distributed according to equation 4.23 with $\chi = \frac{(x-x_0)}{\sigma^2}$ where x is a normal distributed random number.

$$L \sim exp\left(-\frac{\chi^2}{2}\right) \rightarrow -lnL \sim -\frac{\chi^2}{2} \tag{4.23}$$

Since the log-likelihood-value is used in this thesis equation 1 in 4.23 becomes equation 2 in 4.23 after logarithmization. As a next step the ratio LR of the two likelihood-values must determined. It can be written as given in equation 4.24 with a factor of 2 and with the difference of the log-likelihood-functions instead of the ratios of the likelihood-functions.

$$LR = -2 \cdot [ln(L_B) - ln(L_A)] \sim \chi^2 \tag{4.24}$$

The significance in units of σ is then given as in equation 4.25 in a ROOT conform notation. The function *chisquared_quantile_c* is the invers function of the normal distributed χ^2-random number function and $Prob(LR, n_{diffF})$ gives the probability for L to lay outside the confidence interval $\pm\delta = \cdot\sigma$. n_{diffF} denotes the difference between the number of free parameters of the two compared fits.

$$n = \sqrt{chisquared\_quantile\_c(Prob(LR, n_{diffF}), 1)} \tag{4.25}$$

Another important value which gives information about the quality of the fit is the *AICc* value. It is described in [Fri2012]. The *AICc* value considers the number of free parameters of every fit, as well and it needs the *LR* value in the calculation. It is given by equation 4.26 where k denotes the number of free parameters. The *AICc* values of the fit are compared in order to get an evaluation.

$$-LR + 2 \cdot k \tag{4.26}$$

5 Results of the partial wave analysis

The results of the partial wave analysis will be presented in the following sections and subsections of this chapter. As a first step an outline of the base hypothesis will be given which is comprised of the resonances that are clearly visible in the Q-weighted Dalitz-plot discussed in chapter 3. After that hypotheses will be tested with additional resonances like the $\pi_1(1400)$-resonance. The determination of the best hypothesis will depend on the significance of the improvement compared with the prior hypothesis. The last section will present the results for the best hypothesis amongst which will be the contribution of each resonance in the hypothsis, the angle distributions and invariant mass-specra.

5.1 Hypotheses

Before beginning the partial wave analysis some preparations have to be made. The first thing that has to be done is to test a set of hypotheses which might describe the data. The starting point for this is the base hypothesis which is comprised of the resonances in table 5.1 that were found empirically in chapter 3 from the Q-weighted Dalitz-plot. The table lists the masses and the decay widths of the resonances. The values are taken from [PDG2013]. The first two resonances given in table 5.1, the $a_0(980)$ and the $a_2(1320)$, decay into $\pi^{\pm}\eta$. The f_0-resonances, $f_2(1270)$ and ρ_0 decay into the $\pi^+\pi^-$-final state. The dynamics of these resonances are described differently. The dynamics of the resonances $a_2(1320)$, $f_2(1270)$ and ρ_0 are described by a Breit-Wigner-function, the $a_0(980)$ by the Flatte formalism and the contributing f_0-states are described by the $(\pi\pi)_s$-wave via K-Matrix parameterization (see [Ani2002]). Some parameters in the hypotheses are fixed. These parameters are:

- Masses and widths of the resonances
- The pole positions of the f_0-resonances in the $(\pi\pi)_s$-wave

The $(\pi\pi)_s$-wave is comprised of the resonances $f_0(980)$, $f_0(1300)$, $f_0(1500)$, $f_0(1750)$ and the broad state $f_0(1200 - 1600)$.

The hypotheses are fitted to the data using the log-likelihood-method (NLL-function) as an evaluation for the quality of the fit. The fit itself is done gradually, adding new parameters after every fit and comparing the new fit value with the previous value. Another important value of the hypotheses is the highest contributing angular momentum L_{max}. L can be compared with the scattering parameter which is quantized and therefore can only adopt discrete values. L_{max} denotes the highest angular momentum value of the initial $\bar{p}p$-state that still contributes to the process. The fixing of the L_{max}-value in the hypotheses confines the possible set of partial waves. The hypotheses in Table 5.2 will be tested with $L_{max} = 3$. The third hypothesis will be tested for $L_{max} = 4$, as well.

Table 5.1: Set of resonances that constitute the basis for all hypotheses of the partial wave analysis in this chapter. The work from chapter 3, especially the dalitz plot and the invariant mass-spectra with the resonances were the starting point for setting up this set of resonances. The values are taken from [PDG2013]

Resonance	**Mass (MeV/c^2)**	**Decay width (MeV)**
a_0**(980)**	980 ± 20	≈ 50 to 100
a_2**(1320)**	$1318.3\pm^{0.5}_{0.6}$	$105.0\pm^{1.6}_{1.9}$
f_2**(1270)**	1275.1 ± 1.2	$185.1\pm^{2.9}_{2.4}$
ρ	775.49 ± 0.34	146.2 ± 0.7
$(\pi\pi)_s$	Comprised of 5 resonances	—-

.

Table 5.2: The tested hypotheses.

Hypothesis
a_0**(980)**, $(\pi\pi)_s$, f_2**(1270)**, a_2**(1320)**, ρ_0
a_0**(980)**, $(\pi\pi)_s$, f_2**(1270)**, a_2**(1320)**, ρ_0, ω
a_0**(980)**, $(\pi\pi)_s$, f_2**(1270)**, a_2**(1320)**, ρ_0, ω, π_1**(1400)**

5.1.1 Fit values and significances

Using the resonances from table 5.1, a set of three hypotheses can be built which differ in their contributing resonances. The first hypothesis consists of the basis set listed in Table 5.2. The fit-values of this hypothesis will serve as a comparison for the other hypotheses. Its likelihood-value is $NLL = -9669.52$ with $AICc = -18952.7$. It should be noted that the difference between the number of free parameters is important since an improvement of the likelihood-value can always be achieved by adding more free parameters. In order to keep the likelihood-values compareable a value for the goodness of the fit is needed that takes into account the number of free parameters, as well. Two such values exist. These are the $AICc$-value and the significance which was introduced in the previous chapter. The results for the significances are presented later on in this setion. Table 5.3

lists the results for the five tested hypotheses configurations. The table shows five tested hypothses since the third one in Table 5.2 was tested three times with different parameters. It gives the *AICc* values of the fits together with their likelihood-values and number of free parameters. Above each row of values are the resonances and the used L_{max}-values listed. The second hypothesis in Table 5.2 consists of an additional ω resonance without an $\pi_1(1400)$-resonance since the ω might contribute in the data. The third hypothesis in Table 5.2 is with the ω-resonance and with the $\pi_1(1400)$ resonance. The fit for these two resonances was done with a highest contributing angular momentum of $L_{max} = 3$. Hypothesis 2 has 16 more free parameters with 208 than the basis hypothesis with 192 free parameters. Their likelihood-values differ by 69.31 with a value for hypothesis 2 of $NLL = -9738.83$ compared to $NLL = -9669.52$ of the basis hypothesis. The third hypothesis includes both the ω and the $\pi_1(1400)$. The value for L_{max} in the third fit in Table 5.3 is 3 again. The likelihood-value of the fit is -10068.9 which is an improvement of 330 compared to the likelihood-value of the second fit with hypothsis 2. Although fit 3 with hypothesis 3 has with 244 free parameters 36 more than hypothesis 2 in fit 2 the *AICc*-value has improved, as well, with $AIC = -19646.1$. It is an improvement of 588 compared to $AICc = -19058.9$ of hypothesis 2 in fit 2. This is a great indication for the contribution of the $\pi_1(1400)$ and the ω. All hypotheses from 1 to 3 were fit with $L_{max} = 3$. In fit 4 of hypothesis 3 the value for L_{max} is set to 4. The likelihood-value of it is -10204 which is an improvement of 135.3. With 317 free parameters, 73 more than it has in fit 3, the *AICc*-value still improved by 122 to 19768.1. In the last fit in Table 5.3 of hypothesis 3 the masses and decay widths of the resonances described by the Breit-Wigner parameterization are free and not fixed. However, the ω- and ρ_0-resonances stay fixed. The expectation is that if the hypothesis in fit 4 is reasonable than the log-likelihood value should not improve significantly with free parameters of the same fit. Furthermore the masses and widths of the resonances should not drift away from the correct values. The results in Table 5.3 show that the log-likelihood improved by only $= 9.4$ to $NLL = -10213.6$ compared to fit 4. The *AICc* value improved by only 4.4 with 7 more free parameters. These negligible improvements are an indication that hypothesis 3 in fit 4 is reasonable and a good choice.

Apart form the *AICc*-value it is necessary to determine the significances of the improvements between the likelihood-values of the various hypotheses. The formalism for the determination of the significance is introduced in chapter 4. The significances between the various likelihoods are listed in table 5.4. The improvement from hypothesis 1 in fit 1 to fit 2 of hypothesis 2 is $\approx 10\sigma$. According to [PDG2013] this is a significant improvement. Fit 3 compared to 2 is $\approx 23\sigma$ which is an indication for a contribution of an 1^{-+}-wave decaying into $\pi^{\pm}\eta$. A significance of $\approx 10\sigma$ given between the fits 3 and 4 makes $L_{max} = 4$ likely. The fact that the log-likelihood value improved by only $\Delta L = 9.12$ shows that hypothesis 4 is a reasonable correct fit. If it wasn't then the parameters for the masses and widths of the resonances would have drifted apart which didn't happen. The masses and widths

Table 5.3: The fit-values for all hypotheses with $L_{max} = 3$ and $L_{max} = 4$. After every row with the used resonances and L_{max}-values the fit values are listed.

NLL-value	**Number of free parameters**	**AICc-value**
a_0(980), $(\pi\pi)_s$, f_2(1270), a_2(1320), ρ_0	$L_{max} = 3$	
−9669.52	192	−18952.7
a_0(980), $(\pi\pi)_s$, f_2(1270), a_2(1320), ρ_0, ω	$L_{max} = 3$	
−9738.83	208	−19058.9
a_0(980), $(\pi\pi)_s$, f_2(1270), a_2(1320), ρ_0, ω, π_1(1400)	$L_{max} = 3$	
−10068.9	244	−19646.1
a_0(980), $(\pi\pi)_s$, f_2(1270), a_2(1320), ρ_0, ω, π_1(1400)	$L_{max} = 4$	
−10204.2	317	−19768.1
a_0(980), $(\pi\pi)_s$, f_2(1270), a_2(1320), ρ_0, ω, π_1(1400)	$L_{max} = 4$ free parameters	
−10213.6	324	−19772.5

are presented in a subsection later on. As a conclusion it can be said that hypothesis 4 describes the data best.

Table 5.4: Significances of the improvements between the hypotheses. According to the particle data group a value of $\sigma \geq 4$ is significant. The values LR and n_{diffF} are the differences between the hypotheses respective likelihood values and number of free parameters, respectively.

Fit	LR	n_{diffF}	Significance
1 and **2**	69.31	16	9.5σ
2 and **3**	330	36	22.9σ
3 and **4**	135.3	73	10.2σ

5.2 Discussion of the best fit results

5.2.1 Results

The results for the fit of hypothesis 4 will be presented in this subsection which include the Dalitz plots, the invariant-mass-spectra and various angle distributions. The comparison between the Dalitz-plots of the data events and fitted Monte Carlo events is done. The Dalitz plots are depicted in figures 5.1 and 5.2. The first thing one notices in comparing these two dalitz plots is that the fitted plot shows the same resonances as the data plot. In general it can be said that the fitted Monte Carlo events and the data events agree well with one another. Figure 5.3 depicts the invariant mass-spectra. The red lines denote the Monte Carlo fitted events. In 5.3 a) a discrepancy can be seen in the region between $\approx 1\ MeV/c^2$ to $\approx 1.2\ MeV/c^2$. In the spectra in b) and c) no clear discrepancies can be seen. Especially the invariant $\pi^-\eta$ mass spectra of Monte Carlo and data events in c) are nearly one single line. The angle-distributions are shown in figure 5.4. Some of the depicted histograms have greater discrepancies between the Monte Carlo fitted events and data events. Possible Reasons explaning the discrepancies between the fitted events and the data events can be of different kinds. It is possible that the simulated and reconstructed Monte Carlo events have systematic errors. Another possible explanation is that there could be more resonances contributing in the data. The resonances $\rho(1450)$ and $\rho(1700)$ are possible candidates that were not tested in this thesis since the partial wave analysis is very time-consuming. Another explanation could be an error in the detector configuration and calibration. The histograms in figure 5.5 depict various production angles in the $\pi^+\pi^-\eta$-helicity system.

Masses and widths

The masses and resonances that are obtained from the fit of hypothesis 5 are listed in table 5.5. The values correspond to the values in Table 5.1. The values for $a_0(980)$, $a_2(1320)$ and $f_2(1275)$ match with the values of Table 5.1 within their error margins. However, between the values of ρ_0 is a higher discrepancy with $\Delta_{\rho_0} = 10\, MeV/c^2$. The exotic meson $\pi_1(1400)$ has a mass of $m_{\pi_1(1400)} = 1285.03 \pm 0.16\, MeV/c^2$ and a decay width of $\Gamma_{\pi_1(1400)} = 136.03 \pm 0.32$ MeV. The given errors are statistical errors. The average values in [PDG2013] for $\pi_1(1400)$ are $m_{\pi_1(1400)} = 1354 \pm 24\, MeV/c^2$ and $\Gamma_{\pi_1(1400)} = 330 \pm 35\, MeV$.

Table 5.5: Resonance masses and decay widths obtained from the fit with free parameters.

Resonance	**Mass (MeV/c^2)**	**Decay width (MeV)**
a_0**(980)**	981.84 ± 0.19	fitted with Flatte parameterization
a_2**(1320)**	1319.33 ± 0.12	110.28 ± 0.18
f_2**(1270)**	1272.18 ± 0.20	148.06 ± 0.38
ρ	785.49 ± 0.13	151 (fixed)
ω	778.58 ± 0.10	70 (fixed)
π_1**(1400)**	1285.03 ± 0.16	136.03 ± 0.32

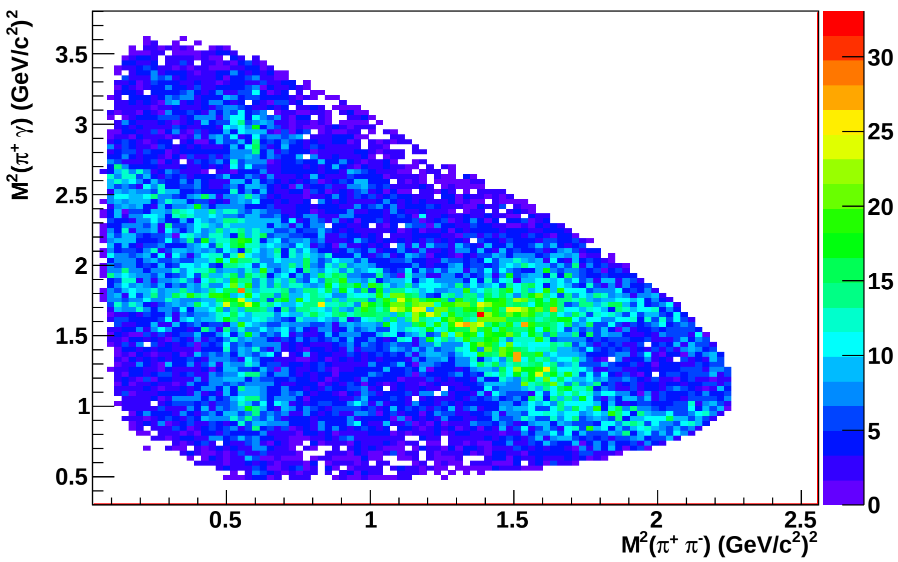

Figure 5.1: Dalitz-plot for the signal events from chapter 3 as a comparison for the dalitz plot of fitted Monte Carlo events in figure 5.2.

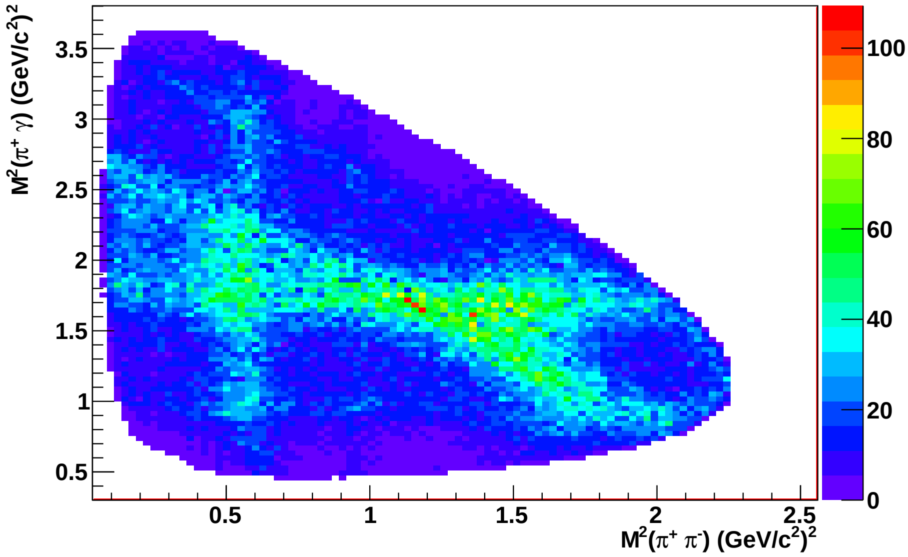

Figure 5.2: Dalitz plot of the fitted Monte Carlo events after the partial wave analysis. The good agreements between the fit and the data can be seen in the same shapes originating from the resonances.

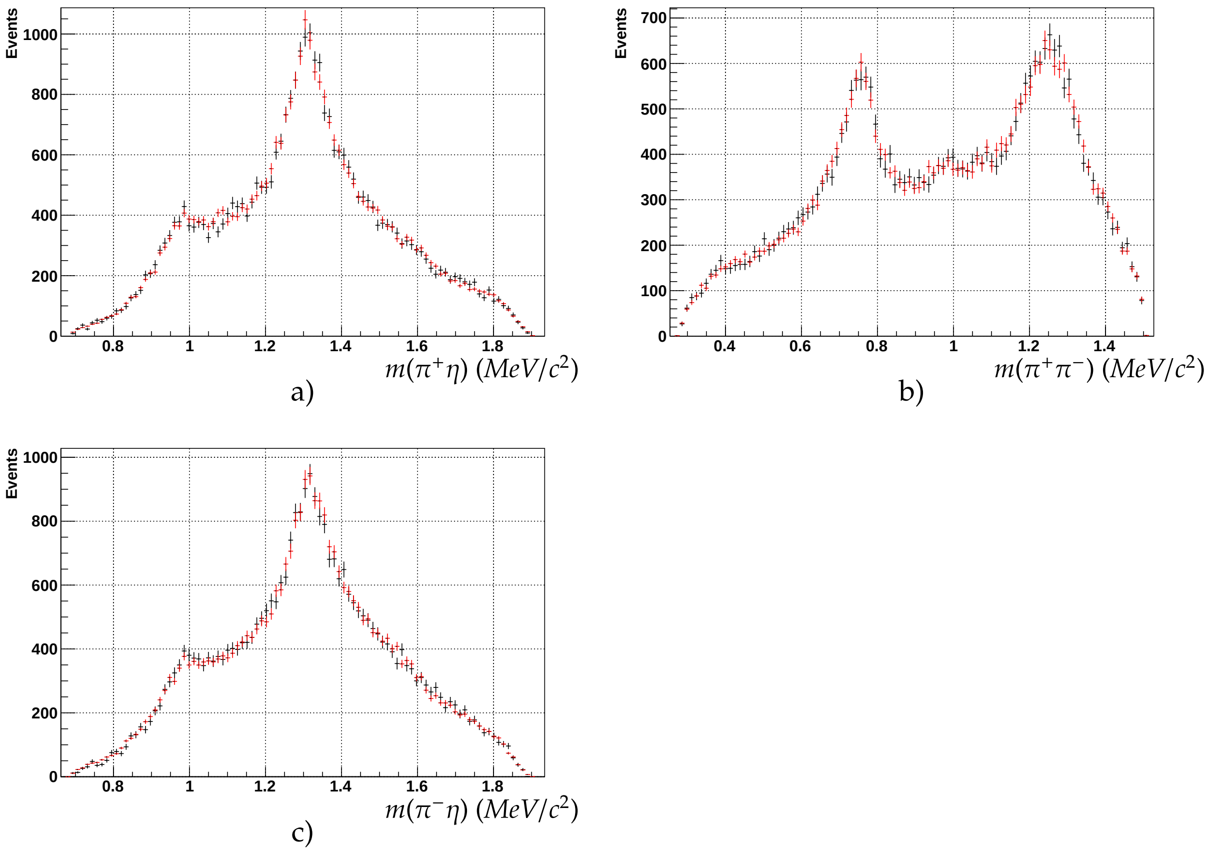

Figure 5.3: Invariant-$\pi^+\pi^-$ and $\pi^\pm\eta$-mass spectra of the data events (black) and the fitted Monte Carlo events. The Monte Carlo fitted events and data events match in their graphs.

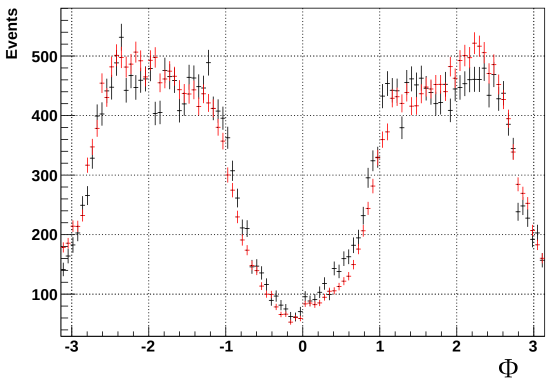

a) Decay angle of η in the $\pi^+\eta$-helicity system

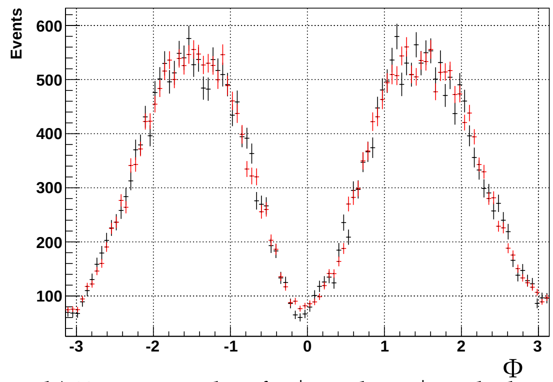

b) Decay angle of π^+ in the $\pi^+\pi^-$-helicity system

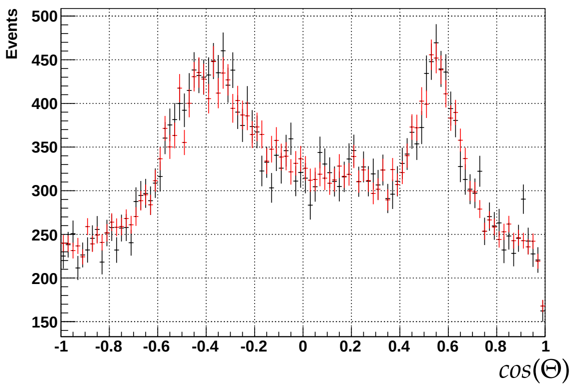

c) Decay angle of η in the $\pi^+\eta$-helicity system

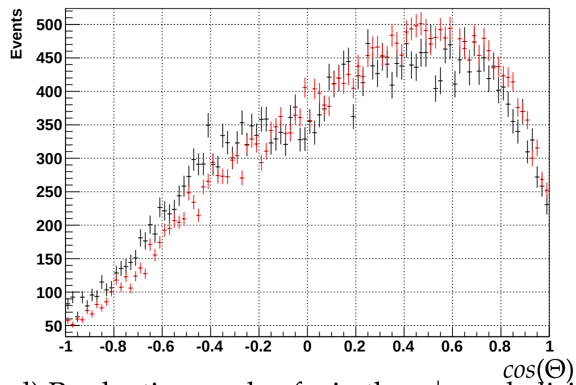

d) Production angle of η in the $\pi^+\pi^-\eta$-helicity system

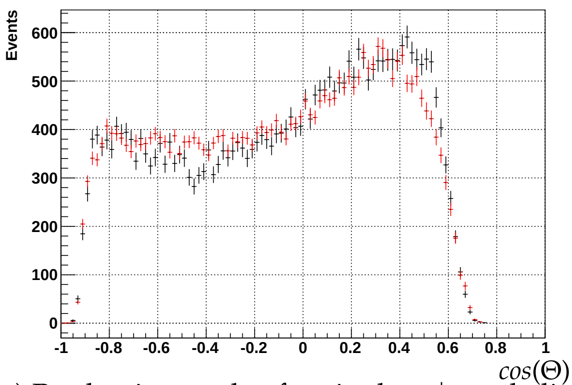

e) Production angle of π^- in the $\pi^+\pi^-\eta$-helicity system

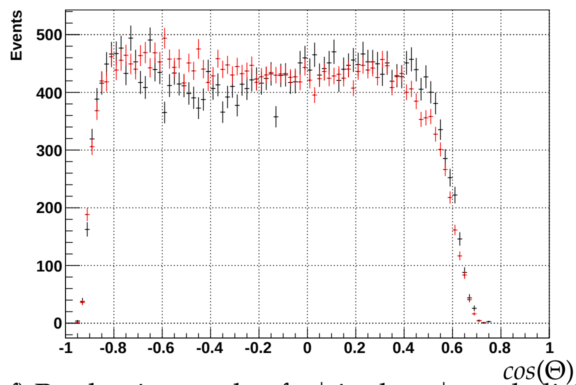

f) Production angle of π^+ in the $\pi^+\pi^-\eta$-helicity system

Figure 5.4: The production and decay angle-distributions of the η (a), c) and d)), the π^- (b) and f)) and the π^- (e)). The text below the histograms gives the helicity system and the angle type.

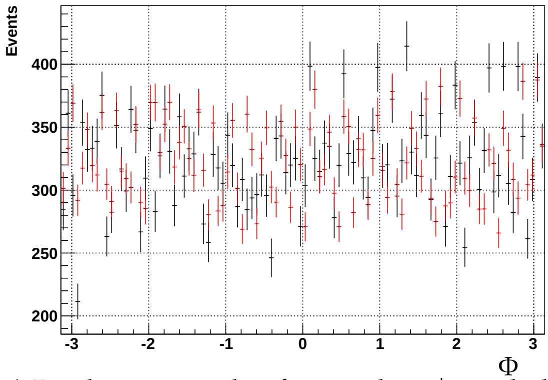

a) Production angle of π^- in the $\pi^+\pi^-\eta$-helicity system

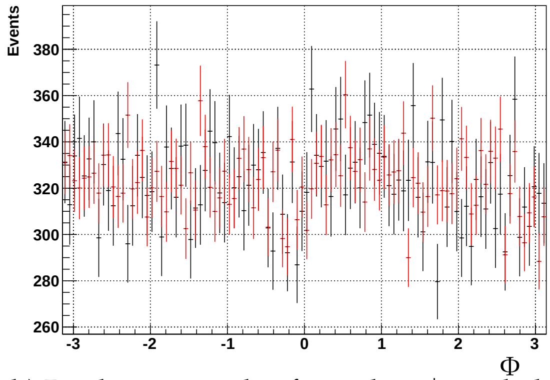

b) Production angle of η in the $\pi^+\pi^-\eta$-helicity system

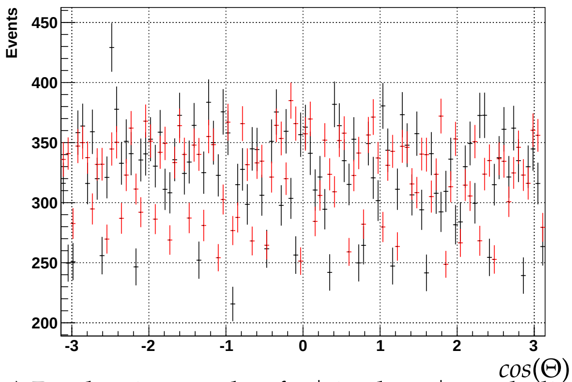

c) Production angle of π^+ in the $\pi^+\pi^-\eta$-helicity system

Figure 5.5: The production angle-distributions of a) the π^-, b) the η and c) the π^+ all in the $\pi^+\pi^-\eta$-helicity system.

5.2.2 Contributions of the resonances

The aim of this subsection is to determine the branching ratios of all resonances in the best fit. The branching ratios are determined by equation 5.1 where $_i$ denotes the contribution of wave i and $_{tot}$ the total wave.

$$B_i = \frac{BF_i}{BF_{tot}} \tag{5.1}$$

The Branching ratios of the resonances with their errors are given in 5.6. The sum of all branching ratios is 155.67% instead of 100% due to interference effects. The highest contributing resonances are $a_0(980)$, $a_2(1320)$ and ρ_0 with $BF_{a_0(980)} = 25.50\%$, $BF_{a_2(1320)} = 30.51\%$ and $BF_{\rho_0} = 25.92\%$. The $\pi_1(1400)$ seems to have a strong contribution with $BF_{\pi_1(1400)} = 22.92\%$. The relatively small contribution of ω with $BF_\omega = 7.56\%$ matches the expectations since the decay mode $\omega \rightarrow \pi^+\pi^-$ has only a small share of $\approx 1.53\%$ of the decay modes of the ω.

Table 5.6: The branching ratios of the resonances in hypothesis 4. The sum of the ratios doesn't have to be 100% due to interferences.

Resonance	**Contribution**	**Error**
$\boldsymbol{a_0}$**(980)**	25.50%	±1.48%
$\boldsymbol{a_2}$**(1320)**	30.51%	±0.01%
$\boldsymbol{f_2}$**(1270)**	17.67%	±0.01%
$\boldsymbol{\pi\pi S - Wave}$	25.78%	±1.44%
$\boldsymbol{\omega}$	7.56%	±1.05%
$\boldsymbol{\rho_0}$	25.92%	±1.77%
$\boldsymbol{\pi_1}$**(1400)**	22.92%	±1.08%
$\boldsymbol{\Sigma}$	155.67%	

6 Summary

The main goal of this thesis was to do a partial wave analysis on the reaction channel $\bar{p}p \rightarrow \pi^+\pi^-\eta$. The data that was subjected to the partial wave analysis had a beam momentum of 900 MeV/c and was taken at the Crystal Barrel Experiment at the research facility CERN in 1996. The data had to undergo the event reconstruction and data selection. In that part of this thesis the data was structured and the background was reduced. In order to reduce the background various methods were used. The most important methods were the kinematic fit and an event based background reduction method which is a relatively new method. It is a multivariate subtraction method. The data was reduced from originally 14875517 down to 44395 after applying all methods and cuts which means that only 6.62% of the data was left for the partial wave analysis. The partial wave analysis was done using the PWA tool that was still in development at the Institut für Experimentalphysik I at the Ruhr-Universität Bochum in Germany during the time of the completion of this thesis. The number of the hypotheses that were used for the fit was 4 all with a basic set of resonances. This set was comprised of several resonances which were the $\boldsymbol{a_0}$**(980)**, $\boldsymbol{(\pi\pi)_s}$-wave with 5 resonances, $\boldsymbol{f_2}$**(1270)**, $\boldsymbol{a_2}$**(1320)** and the $\boldsymbol{\rho_0}$. An ω-resonance was also added and improved the log-likelihood-value significantly with $NLL = -9669.52$. The highest contributing angular momentum of the $\bar{p}p$-system was set at $L_{max} = 3$. An addtional $\pi_1(1400)$-resonances led to a significant improvement of $\approx 22.87\sigma$ compared to the hypothesis with the ω. Hypothsis 4 with $L_{max} = 4$ and an extra ω- and $\pi_1(1400)$-resonance proved to be the best fit. The number of free parameters was 317, $NLL = -10204.2$ and $AICc = -19768.1$. The branching ratio of the $\pi_1(1400)$-resonance in that fit was 22.92%. The mass and decay width of $\pi_1(1400)$ were found to be $m_{\pi_1(1400)} = 1285.03 \pm 0.16\ MeV/c^2$ and $\Gamma_{\pi_1(1400)} = 136.03 \pm 0.32\ MeV/c^2$.

A Dalitz plot

This section will give an introduction to the Dalitz-plot and its formalism based on the introduction given in [Schmi1996]. The dalitz plot is named after Richard Dalitz and is a method to visualize the kinematic information of events that are made of three particles. The dalitz plot gives indicationd on intermediate states of final states through the resonances that can be seen in it (figure A.1). The reaction probability for a three particle system is:

$$\sigma \propto \int |M|^2 dLIPS \tag{A.1}$$

The M is the transition matrix of the three-particle process and LIPS is the lorentz invariant phacespace given by

$$LIPS = \int \frac{d^3p_1}{2E_1}\frac{d^3p_2}{2E_2}\frac{d^3p_3}{2E_3}\delta^4(P - \sum_{i=1}^{3} p_i) \tag{A.2}$$

After applying energy and momentum conservation the independant variables reduce to only E_1 and E_2 the energies of the center of mass systems of particles 1 and 2:

$$LIPS = Norm \int dE_1 dE_2 \tag{A.3}$$

The conclusion of A.10 is that the complete kinematic information of any event is contained in the E_1-E_2-plane. It is common to use the squared invariant masses m_{12}^2 and m_{13}^2 instead of using the center of mass energies E_1 and E_2. The index 12 and 13 denote the combination of the particle with $m_{12}^2 = m_1^2 + m_2^2$ and $m_{13}^2 = m_1^2 + m_3^2$. The masses can be obtained from the momentums of the particles. As an example the dalitz plot for $\pi^+\pi^-\eta$ events is depicted in figure A.1.

In a dalitz plot all physical events are within a triangle shape. The shape of the triangle is limited by various kinematic constraints. The limits can be obtained as follows: In the plot in figure A.1 the squared invariant $\pi^+\pi^-$-masses are on the x-axis and the squared invariant $\pi^+\eta$-masses are on the y-axis. Then the boundarie for the x-axis are

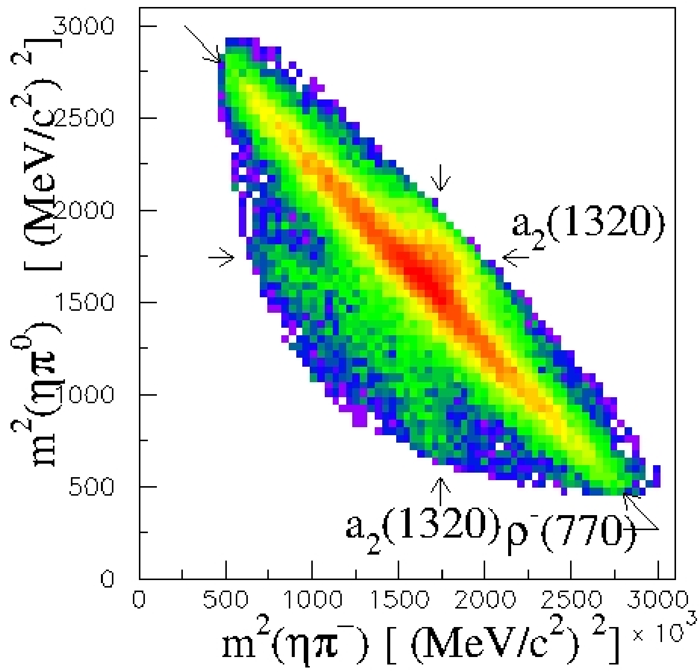

Figure A.1: Example dalitz plot of $\pi\eta$. Changing densities are an indication for resonances. The figure is from [CB2013].

$$m^2_{min,\pi^+\pi^-} = (m_{\pi^+} + m_{\pi^-})^2 \tag{A.4}$$
$$m^2_{max,\pi^+\pi^-} = (E_{tot} + m_{\pi^-+})^2 \tag{A.5}$$

and for the y-axis

$$m^2_{min,\pi^+\eta} = (m_{\pi^+} + m_{\eta})^2 \tag{A.6}$$
$$m^2_{max,\pi^+\eta} = (E_{tot} + m_{\pi^+})^2 \tag{A.7}$$

The last boundary that limits the vertical to the bisector is given as

$$m^2_{min,\pi^+\pi^+} = (2m_{\pi^+})^2 \tag{A.8}$$
$$m^2_{max,\pi^+\eta} = (E_{tot} + m_{\eta})^2 \tag{A.9}$$

At last the dalitz plot itself is bound by the constraint

$$m^2_{1,2} + m^2_{1,3} + m^2_{2,3} = const. = s + m^2_1 + m^2_2 + m^2_3 \tag{A.10}$$

with $m_{i,j}$ explained above and $s = E_{tot}^2$ the Mandelstam-variable. Furthermore it is one can extract the decay angle for a particle decaying into two different particles according to

$$cos\Theta = \frac{2m_{i,j}^2 - (m_{i,j,min}^2 + m_{i,j,max}^2)}{m_{i,j,min}^2 - m_{i,j,max}^2} \tag{A.11}$$

The variables $m_{i,j,min}$ and $m_{i,j,max}$ set the boundaries for the mass range of the resonance that is of interest.

B Bibliography

[Ani2002] V. V. Anisovich and A. V. Sarantsev: *K matrix analysis of the* $(I\ J^{PC} = 00^{++}) - waveinthemassregionbelow1900MeV, Eur.\ Phys.\ J.\ A\mathbf{16}(2003)229[hep - ph/0204328]$.

[Beu1995] Beuchert, Karsten: *Untersuchung zur $\overline{p}p$-Annihilation im Fluge am Crystal-Barrel-Detektor*, Ruhr-UniversitÃt Bochum, Dissertation, 1995).

[CB2013] The Crystal Barrel Server: URL: `http://www-meg.phys.cmu.edu/cb/` [Status: 01.10.2013]

[CBL1992] The CRYSTAL BARREL Collaboration (E. Aker et al.): *The Crystal Barrel Detector at LEAR*. Nucl. Instrum. Methods A321, 69, (1992), CERN-PPE/92-126.).

[Fri2012] Friedel, Patrick: *Analyse des Zerfalls $J/\Psi \rightarrow \gamma\phi\phi$ bei BESIII und Entwicklungen fÃ$\frac{1}{4}$r den Prototyp des $\overline{P}ANDA - EMC$*, Ruhr-Universität Bochum, Dissertation, 2012).

[Kra2012] Krah, Sebastian: *Entwicklung von Testsystemen zur Charakterisierung von Silizium-Streifen-Detektoren*, Rheinische Friedrich-Wilhelms-Universität Bonn, Diploma Thesis, 2012).

[Kur1995] Kurilla, Udo: *Untersuchungen zur Partialwellenanalyse der Reaktion $\overline{p}p \rightarrow \omega\pi^0$*, Ruhr-Universität Bochum, Master Thesis, 2012).

[Mar2009] Martin, Brian: *Nuclear and Particle Physics: An Introduction*, John Wiley Sons, 2., 2009).

[PAN2009] PANDA Collaboration: *Physics Performance Report.* In: http://arxiv.org/abs/0903.3905v1 ; 2009).

[PDG2013] Particle Data Group: URL: `http://pdg.lbl.gov/` [Status: 01.10.2013]

[Pov2009] Povh, B.; Rith, K.; Scholz, C.; Zetsche, F.: *Teilchen und Kerne: Eine EinfÃ$\frac{1}{4}$hrung in die physikalischen Konzepte*, Springer, 8., 2009).

[Pyc2012] Pychy, Julian: *Untersuchungen zur Partialwellenanalyse der Reaktion $\overline{p}p \rightarrow \omega\pi^0$*, Ruhr-Universität Bochum, Master Thesis, 2012).

[Ric84] Richman, Jeffrey D.: *An Experimenterâs Guide to the Helicity Formalism*, CALT-68-1148 DOE RESEARCH AND DEVELOPMENT REPORT, 1984).

[Schmi1996] Schmidt, Peter W. E.: *Partialwellenanalyse der Proton-Antiproton-Annihilation im Fluge in* $K^{+}K^{-}\pi^{0}$, Universität Hamburg, Dissertation, 1996).

[Schul2000] Schulten, K.: *Notes on Quantum Mechanics*, Department of Physics and Beckman Institute University of Illinois at UrbanaâChampaign, 2000).

[Schul2012] Schulze, Jan: *Analyse des Zerfalls* $\chi_{c0} \rightarrow KK^{-}\pi^{0}\pi^{0}$ *bei BESIII und Entwicklung von mechanischen Komponenten für einen Prototypen des PANDA-EMC*, Ruhr-Universität Bochum, Dissertation, 2012).

[Kie1994] Kiel, Torsten: *Untersuchung der* ω*- und der* Φ*- Produktion in der Proton-Antiproton- Annihilation*, Universität Hamburg, Dissertation, 1994).

[WIL2009] Williams, M.; Bellis, M.; Meyer, C. A.: *Multivariate side-band subtraction using probabilistic event weights.* In: http://arxiv.org/abs/0809.2548 ; 2009).

[WIL2007] Williams, Mike: *Measurement of Differential Cross Sections and Spin Density Matrix Elements along with a Partial Wave Analysis for* $\gamma p \omega$ *using CLAS at Jefferson Lab*, Carnegie Mellon University , Dissertation, 2007).

C Acknowledgements

First of all, I would like to thank Prof. Dr. Ulrich Wieder who gave me the opportunity to write my Master Thesis at his institute "Institut für Experimentalphysik I".

I am specially grateful to my Master's Thesis advisor Dr. Bertram Kopf who supported me in physical and technical questions during my whole work.

I want to thank Dr.Thorsten Schröder and Julian Pychy who gave me many useful advices. Furthermore I want to thank PD Dr. Fritz-Herbert Heinsius for taking on the second report of my Master Thesis.

I want to thank my family for supporting me in times of hardships. Without them this thesis would have been impossible for me to write.

At last I want to direct my thanks to all others who supported me and contributed to the success of this Thesis.

Erklärung

Ich versichere, dass ich die vorliegende Arbeit selbstständig angefertigt und mich fremder Hilfe nicht bedient habe. Alle Stellen, die wörtlich oder sinngemäß veröffentlichtem oder unveröffentlichtem Schrifttum entnommen sind, habe ich als solche kenntlich gemacht. Die Arbeit wurde bisher keiner anderen Prüfungskommission in gleicher oder ähnlicher Form von mir vorgelegt.

Bochum, 16.10.2013

Erdem Köz